Sheath Formation Around a Dielectric Droplet in a He Atmospheric Pressure Plasma

Mackenzie Meyer[1], Gaurav Nayak[2], Peter J. Bruggeman[2], Mark J. Kushner[3,4]

[1] University of Michigan, Applied Physics Program, Ann Arbor, MI 48109-1040 USA maemeyer@umich.edu
[2] University of Minnesota, Department of Mechanical Engineering, Minneapolis, MN, 55455 USA nayak025@umn.edu:, pbruggem@umn.edu
[3] University of Michigan, Electrical Engineering and Computer Science Department, 1301 Beal Ave., Ann Arbor, MI 48109-2122 USA mjkush@umich.edu
[4] Author to whom correspondence should be addressed.

Abstract

Interactions at the interface between atmospheric pressure plasmas and liquids are being investigated to address applications ranging from nanoparticle synthesis to decontamination and fertilizer production. Many of these applications involve activation of droplets wherein the droplet is fully immersed in the plasma and synergistically interacts with the plasma. To better understand these interactions, 2-dimensional (2D) modeling of radio frequency (RF) glow discharges at atmospheric pressure operated in He with an embedded lossy dielectric *droplet* (tens of microns in size) was performed. The properties of the sheath that forms around the droplet were investigated over the RF cycle. The electric field in the bulk plasma polarizes the dielectric droplet while the electron drift in the external electric field is shadowed by the droplet. The interaction between the bulk and sheath electric fields produces a maximum in E/N (electric field/gas number density) at the equator on one side of the droplet where the bulk and sheath fields are aligned in the same direction and a minimum along the opposite equator. Due to resistive heating, the electron temperature T_e is maximum 45° above and below the equator of the droplet where power deposition per electron is the highest. Although the droplet is, on the average, negatively charged, the charge density on the droplet is positive on the poles and negative on the equator, as the electron motion is primarily due to diffusion at the poles but due to drift at the equator.

I. Introduction

Interactions between atmospheric pressure plasmas and liquids are being investigated for applications such as plasma medicine and water treatment [1–4]. The plasma produces reactive oxygen and nitrogen species (RONS) that solvate into the liquid to chemically activate the fluid. This chemical activation can remediate complex organic molecules in the liquid such as benzene or methyl blue dye [5,6]. These reactive species have also been shown to reduce viability of bacteria and cancer cells [7–9].

The interaction of plasmas and liquids is actively being studied, with emphasis on both short-lived and long-lived reactive species. Modeling by Heirman et al has shown that only limited RONS (H_2O_{2aq}, HNO_{2aq} and $NO_2^-{}_{aq}$, and HNO_{3aq} and $NO_3^-{}_{aq}$) are present in solutions in large concentrations 15 s after plasma exposure [10]. (The "aq" subscript indicates a solvated or in-liquid species.) Short-lived RONS such as OH_{aq} react quickly at the plasma-liquid interface, while other long-lived RONS such as HO_{2aq}, $ONOOH_{aq}$, and O_{3aq} react or de-solvate into the gas phase within 10 s of liquid exposure, though these times scales are system dependent. De-solvation occurs most rapidly for systems having a large surface-to-volume ratio, such as droplets. We note that species may be continually generated, but reactive species may have low concentrations. Roy et al experimentally observed RONS formation in a filamentary dielectric barrier discharge operated at varying N_2/O_2 fractions where the water was in contact with the ground electrode [11]. They found that the $NO_3^-{}_{aq}$ density in the liquid increases as the fraction of O_2 in the gas increases as O_{aq}, $O_2^-{}_{aq}$, and O_{3aq} are precursors to $NO_3^-{}_{aq}$.

Plasma-induced electrochemistry also depends on the transport of plasma-produced species into solutions. For example, nanoparticles can be produced in metal ion containing solutions exposed to atmospheric pressure plasmas. Zheng et al showed that in an $AgNO_{3aq}$ solution, neutral Ag_{aq} clusters form when the solvated electron concentrations are higher than the $Ag^+{}_{aq}$ concentration, and Ag_{aq} ion clusters form when the reverse is true [12]. Other studies have focused on processes at the interface between the plasma and the liquid. Akiyama et al performed Monte Carlo simulations to determine how far electrons penetrate into water before they become solvated electrons. They showed that solvated electrons can be produced 17 nm from the water surface for incident electron energies relevant to atmospheric pressure plasmas [13].

Transport is the limiting factor in chemical activation of liquids as the plasma generated RONS need to transport to the interface of the gas and liquid and then diffuse into the bulk liquid.

These transport limitations can be mitigated to some degree. A high surface-to-volume ratio (SVR) of the liquid can shorten the time the RONS require to diffuse from the interface to the bulk liquid. Another mitigation strategy is to form the RONS very close to the liquid surface, shortening the distance between the RONS and the interface.

Previous studies have examined these transport limits at the interface. Liu et al varied the surface to volume ration (SVR) of water and found that the concentration of long-lived RONS (H_2O_{2aq}, $NO_2^-{}_{aq}$, $NO_3^-{}_{aq}$, and $H^+{}_{aq}$) increased as the SVR increased [14]. In particular, $NO_2^-{}_{aq}$, $NO_3^-{}_{aq}$, and $H_3O^+{}_{aq}$ increased nearly linearly with SVR, while the density of H_2O_{2aq} saturated at higher SVRs. Hassan et al investigated the transport of H_2O_2 and O_3 into electrosprayed water droplets [15]. While H_2O_{2aq} and O_{3aq} concentrations in the droplets increased with treatment time, the H_2O_{2aq} concentration was 4 orders of magnitude larger than O_{3aq}, due to the higher Henry's law constant of H_2O_2. While O_{3aq} in the liquid reached saturation without coming close to depleting the gas phase, H_2O_2 in the gas phase was depleted before the liquid became saturated. The total surface area of the droplets also increased H_2O_{2aq} and O_{3aq} concentrations in the liquid. Delgado et al used a 1-dimensional reaction-diffusion model to investigate a general transport limited reaction involving solvated electrons and a general scavenger represented by S ($e_{aq} + S^n \rightarrow S^{n-1}$) [16]. Once S at the surface is depleted, the reaction becomes transport limited as S must diffuse to the surface of the liquid. To increase the yield of the scavenger reaction, they suggest pulsing the plasma, decreasing the electron flux, and using a multiphase system where the liquid is interspersed in the plasma. Silsby et al used a global model to investigate one-film and two-film transport theory at the interface between the gas and liquid [17]. Using Sherwood numbers (ratio of convective mass transfer to diffusive mass transfer) specific to each species, they showed that two-film transport theory more accurately captures the gas-liquid interface than one-film transport theory.

In this investigation, atmospheric pressure plasma interactions with dielectric *droplets* as a proxy for liquid droplets were computationally investigated for a radio frequency (RF) plasma sustained in helium. This study builds on previous experimental work in the same system to investigate transport processes into liquid droplets. The experimental system had a 2 mm gap between electrodes and electrode length of 9.5 mm [18]. To characterize the plasma, Nayak et al measured He metastable densities produced by broadband absorption spectroscopy [18]. They found that the densities of both He metastables $He(2^3S)$ and He_2^* were maximum close to the

electrodes. Adding 50 ppm of H_2O to the gas mixtures reduces both monomer and dimer He excited state densities due to quenching by H_2O. In a companion study, Nayak et al used broad-band absorption and optical emission spectroscopy to estimate the electron temperature and density for both He and Ar plasmas [19]. They measured the plasma emission and estimated the emissivity using Maxwellian and non-Maxwellian electron energy distributions (EEDs). The best fit of the emissivity was found with a non-Maxwellian EED which produced an electron temperature of 3.5 eV and electron density of 1.2×10^{11} cm^{-3} for a He plasma. Having characterized the plasma, Oinuma et al investigated the transport of OH into a water droplet by flowing water droplets through the plasma and collecting them for later analysis [20]. Formate ($HCOO^-_{aq}$) was dissolved in the droplet, and its degradation over time provided an estimate of OH radicals solvating into the droplet from the plasma. Based on a 1-dimensional reaction-diffusion model that matches the experimental results, OH_{aq} reacts with $HCOO^-_{aq}$ primarily at the surface of the droplet. $HCOO^-_{aq}$ degradation is therefore limited by $HCOO^-_{aq}$ diffusion from the bulk to the surface of the droplet. The effects of other reactive species, including O, H, $O_2(a^1\Delta_g)$, O_3, metastable He atoms, and metastable Ar atoms, on $HCOO^-_{aq}$ degradation were analyzed by Nayak et al [21]. O was found to possibly contribute to the degradation of $HCOO^-_{aq}$, and a lower bound on that reaction rate was estimated to be 1.66×10^{-13} cm^3/s.

The plasma treatment of liquid droplets affects the surrounding in several ways. The droplet will likely evaporate, producing a region of high vapor density around the droplet that will affect plasma transport properties and plasma chemistry. The droplet may act as a sink for plasma-produced reactive species or a source of in-liquid produced species which transport into the plasma. The droplet is also electrically active. That is, the droplet will electrically charge as a floating body in a plasma, producing a sheath at its boundary with the plasma. Droplets with large electrical permittivities will polarize in the applied and plasma generated electric fields. The polarization electric fields then modify plasma properties.

The plasma chemistry and electrical consequences of droplets in plasmas occur simultaneously. In order to investigate and isolate the electrical consequences of droplets in atmospheric pressure plasmas, the results discussed here focus on the plasma-surface interactions of a dielectric, non-reactive droplet. The system is an atmospheric pressure RF generated plasma sustained in He, similar to the experiments conducted by Nayak et al and Oinuma et al [18–21]. We found that the sheath around the droplet is asymmetric due to the horizontally applied electric field and

polarization of the droplet. While the sheath oscillates over the RF cycle, the applied voltage and sheath oscillation are 50-60° out of phase, a consequence of the RC-like behavior of the current flow (capacitance due to sheaths and the droplet, and resistivity due to the bulk plasma). The electric field around the droplet is the sum of the electric field in the bulk plasma resulting from the applied voltage, the sheath electric field surrounding the droplet, and the electric field due to polarization of the dielectric droplet. This combination produces a maximum in E/N (electric field/gas number density) on one side of the droplet, where these electric fields constructively interfere, and a minimum in E/N on the opposite side of the droplet, where these electric fields destructively interfere. Changing the relative permittivity ε_r, diameter, and conductivity of the droplet primarily affects the sheath surrounding the droplet by changing the polarization and allowing charge transport through the droplet.

The conditions for the study and model are described in Sec. II. Comparison of the model to experimental results of plasma properties are presented in Sec. III. The bulk plasma properties and properties of the sheath surrounding the droplet are described in detail in Sec. IV. Results of varying the properties of the droplet (relative permittivity ε_r, diameter, conductivity) are discussed in Sec. V, and results of varying properties of the plasma (RF frequency, power deposited) discussed in Sec. VI. Concluding remarks are in Sec. VII.

II. Description of the Model and Experiment

The conditions investigated in this study are patterned after the experiments conducted by Nayak et al and Oinuma et al [18–21]. The reactor is an atmospheric pressure RF glow discharge sustained in He and operated at 13.56 MHz. The two parallel plate electrodes are separated by 2 mm and are surrounded by polytetrafluoroethylene (Teflon). As described by Oinuma et al [20], water droplets (36 μm – 56 μm in diameter) are dispensed and flow with the gas through the reactor for fundamental studies of plasma-droplet interactions. These droplets are collected by an aluminum insert kept at a temperature below freezing to preserve the droplets for later chemical analysis.

To investigate the sheath that forms around the droplet immersed in the RF plasma, the 2-dimensional (2D) model *nonPDPSIM* was used. *nonPDPSIM* is described in detail by Norberg et al [22] and so will be only briefly discussed here. *nonPDPSIM* addresses the transport of charged and neutral particles and plasma dynamics on an unstructured mesh. Poisson's equation for the electric potential and the continuity equations for charged species densities and charge in or on

materials are implicitly and simultaneously integrated in time using an iterative Newton-Raphson method. Charged particle fluxes are determined by the Scharfetter and Gummel method [23]. Secondary electron emission from surfaces in contact with the plasma was included with a yield for all positive ions of 0.1 on metal surfaces and 0.01 on dielectric surfaces. With the plasma being largely confined between the metal electrodes, the plasma properties are not particularly sensitive to the value of the secondary electron emission coefficient on the bounding dielectrics. The temperature of these secondary electrons was assumed to be the electron temperature at that location.

The electron temperature T_e is determined by an electron energy conservation equation that is implicitly solved using the successive-over-relaxation method after each time step update of the charged particle densities and electric potential. Updates to neutral species densities are then performed using their individual continuity equations. Electron-impact rate coefficients were determined by solving the stationary Boltzmann's equation for electron energy distributions for a range of electric field/gas number density (E/N). A table of electron-impact rate and transport coefficients as a function of the mean electron energy (or temperature) was then constructed. This table was interpolated during execution of the code. The table was updated every 5 ns during integration of the plasma transport equations to reflect changes in composition of the gas. Photoionization was not included.

Total power was determined by computing the RF cycle average over the period τ of the volume integral of current density times electric field.

$$P = \frac{1}{\tau}\int_0^\tau \int \vec{j}\left(\vec{r},t\right)\cdot\vec{E}\left(\vec{r},t\right)d^3r\,dt \qquad (1)$$

In order to obtain the desired power deposition, the applied voltage was adjusted following each RF cycle. A quasi-steady state power was typically produced after 20 cycles of adjusting voltage, depending on the goodness of the initial estimate of voltage amplitude.

Two geometries for the atmospheric pressure RF glow discharge were investigated in this work. The first 2D Cartesian geometry closely replicated the experimental reactor and is shown in Figs. 1a and 1b. The droplet is not included in this geometry to better compare model results with experimental measurements of the plasma. The mesh contains 9,077 total nodes and 6,379 gas phase nodes. The left electrode and boundary of the computational domain were grounded. The right electrode and boundary of the computational domain were powered. The electrodes are separated by 2 mm. The Teflon ($\varepsilon_r = 2.1$) above and below the electrodes is separated by 3 mm.

The depth of the reactor was 1.91 cm. To compare with experiments, the plasma was sustained in He with air impurities (6 ppm N_2, 2.3 ppm H_2O, and 1.5 ppm O_2), and the RF frequency was 13.56 MHz [18].

The second 2D geometry was used to investigate the sheath around the droplet and is shown in Fig. 1c. The numerical mesh has 9,695 total nodes and 7,344 gas phase nodes. This 2D Cartesian geometry was similar to the experimental reactor with the exception of the electrode gap which was increased to 3 mm. The gap between the Teflon above and below the electrodes was 4 mm. The increase in the gap was made to better isolate the sheath dynamics around the droplet from the sheath dynamics occurring at the electrodes. The depth of the reactor was 1.91 cm. The plasma was sustained in He with dry air impurities (16 ppm N_2 and 4 ppm O_2). The RF frequency was 10 MHz or 50 MHz, and the power deposition was varied from 1 W to 15 W. Evaporation from the droplet is not included in the model. The model was typically executed for over 135 cycles in each case to achieve quasi-steady state over an RF cycle.

A dielectric droplet was placed at the center of the gap between the electrodes with its diameter varied from 40 μm to 80 μm. The numerical mesh near the droplet is shown in Fig. 2. The relative permittivity ε_r of the droplet was varied from 1 to 80, and the conductivity was varied from 0 to 10^{-1} S/cm. The droplet is treated as a dielectric as opposed to an active liquid plasma. This choice was made in order to isolate the sheath dynamics which are more universal behavior from the plasma-chemical processes that may be particular to a given system. Since we used a 2D Cartesian geometry, the droplet is effectively represented as a cylindrical rod in the model. The differences caused by the droplet being a cylinder as opposed to a sphere in the experiment are mentioned during discussion of the results.

The reaction mechanism consisted of 15 charged species, 11 neutral species, and 18 excited states with 796 reactions. The species included in the model are listed in Table 1. A limited number of oxygen and nitrogen species were included to account for the dry air impurities. Given their small densities, higher order species such as nitrogen oxides were not included in the mechanism. The reaction mechanism was based on Van Gaens and Bogaerts [24] with updates to include He made by Norberg [25]. Updates based on branching ratios to excited states of recombination of He^+ and He_2^+ were obtained from Emmert et al [26], and radiation trapping factors were computed in the manner described by Lietz [27].

III. Comparison of Results from the Model to Experiments

Predictions of the model were compared to the results of experiments performed by Nayak et al [18,19]. These experiments measured the electron density and temperature as well as the density of the metastable states He(2^3S) and He_2^*. These measurements were made without water droplets in the plasma. The power deposition was 15 W at an RF frequency of 13.56 MHz.

The bulk plasma properties obtained from the model are shown in Fig. 3a time-averaged over one quasi-steady state RF cycle – electron density, E/N and T_e. The electron density peaked at the sheath edge at the electrodes (8.7×10^{11} cm^{-3}) with the density in the center of the gap a factor of two lower (4×10^{11} cm^{-3}). This profile is enabled by dissociative recombination of molecular ions in the bulk plasma dominating electron loss. With the electron density peaking near the sheath edge, this plasma may operating in a combination of a γ-mode or a Penning mode [28,29]. In the γ-mode, ionization is dominated by secondary electron emission, acceleration in the sheaths at the electrodes and subsequent electron impact ionization. The Penning mode produces ionization in the sheaths by Penning ionization from excited states produced in the sheath. For these conditions, the time averaged rate of direct electron impact ionization in the sheaths has a maximum value of 1.6×10^{18} cm^{-3}s^{-1}. The rate for Penning ionization is 4.1×10^{18} cm^{-3}s^{-1}.

E/N peaks in the sheaths at the electrodes with a maximum value of 30 Td (1 Td = 10^{-17} V-cm^2), while E/N in the bulk plasma is an order of magnitude lower at 2 Td. The sheath thickness at the electrodes is about 300 μm on a time-averaged basis. Since T_e is largely determined by E/N, T_e also peaks in the sheaths near the electrodes at 4 eV while T_e in the bulk plasma is 1.5 eV. These results mirror those for modeling atmospheric pressure He capacitively coupled discharges having similar gaps and power deposition [28,30–32]. The power deposition also peaks in the sheaths near the electrodes. T_e at various times throughout the RF cycle is shown in Fig. 3b across the plasma gap. This profile across the plasma gap is taken at the center of the electrodes. At 18.4 ns (25% through the RF cycle when the powered electrode is at its peak voltage), T_e reaches 6.5 eV near the grounded electrode and is 1.1 eV near the powered electrode. The maximum T_e in the bulk plasma is 1.8 eV. The opposite is true at 52.3 ns (75% through the RF cycle) when the voltage on the powered electrode is at its most negative. The time-averaged T_e is also shown in Fig. 3b.

To determine the electron density and T_e, Nayak et al measured the absolute optical emission from the plasma. They calculate the emissivity due to Bremsstrahlung as a function of wavelength, $\varepsilon_{ea}(\lambda)$, from

$$\varepsilon_{ea}(\lambda) = C_{ea}\frac{n_e[He]}{\lambda^2}\int_{\frac{hc}{\lambda}}^{\infty}\sigma_m(\varepsilon)\varepsilon^{3/2}\left(1-\frac{hc}{2\lambda\varepsilon}\right)\sqrt{1-\frac{hc}{\lambda\varepsilon}}f(\varepsilon)d\varepsilon, \quad (2)$$

where λ is the emission wavelength, ε is the electron energy, C_{ea} = 1.77 W m^2 J$^{-3/2}$ sr^{-1}, n_e is the electron density, [He] is the He density (2.45 × 10^{19} cm^{-3}), h is Planck's constant, c is the speed of light, $\sigma_m(\varepsilon)$ is the momentum transfer cross section for electrons colliding with He [33], and $f(\varepsilon)$ is the electron energy distribution. They compared these emissivity estimates to their experimentally measured emission spectra to determine n_e and T_e. These values of n_e and T_e are temporal and spatial averages over the volume from which photons were collected over the RF cycle.

To compare results of the model to the temporal and spatially averaged experimental results, the emissivity at discrete points across the plasma gap was calculated by using time-resolved n_e and T_e at each location across the gap, as provided by the model, and a Maxwell-Boltzmann electron energy distribution, which is a simplifying assumption. The emissivity was only calculated for those locations with electron temperatures above 1.37 eV (energy of a 900 nm photon, lowest wavelength measured). The emissivity was then averaged over time and across the plasma gap. The predicted emissivity from the model is shown in Fig. 4a. Experimentally, the electron density and temperature required to reproduce measured emissivity are n_e = 2.0 × 10^{11} cm^{-3} and T_e = 2.5 eV when using a Maxwell-Boltzmann energy distribution [19]. The emissivity predicted by the Maxwell-Boltzmann energy distribution is also shown in Fig. 4a. The best fit reported by Nayak et al was for a non-Maxwellian energy distribution (1.2 × 10^{11} cm^{-3} and 3.5 eV). As shown in Fig. 4a, the emissivity predicted by the model closely matches the experimental results, indicating that the model accurately represents the experimental conditions.

Measurements were also made of the densities of two He metastable states (He(2^3S) and $He_2(a^3\Sigma_u^+)$) [18]. The densities predicted by the model are compared to the experimental measurements in Fig. 4b. The time-averaged densities from the model results were extracted along a line perpendicular to the electrodes and at the center of the electrode height. The modeled densities were also smoothed by averaging within 0.2 mm. To estimate the value of $He_2(a^3\Sigma_u^+)$ from the lumped He_2^* state in the model, the density of He_2^* is multiplied by the fraction of He(2^3S) divided by the total He excited state density, since He(2^3S) forms $He_2(a^3\Sigma_u^+)$ at each point across the plasma gap. Both He metastable densities from the model are maximum near the electrodes and decrease by at least three orders of magnitude in the bulk plasma due to the higher T_e near the electrodes and quenching of these states by impurities. The experimentally measured densities are

normalized to span the entire plasma gap. The experimentally measured densities are also maximum close to the electrodes and decrease significantly in the bulk plasma. The model results reproduce the spatial dependence of the densities measured in the experiments, albeit with higher maximum densities. The difference in peak densities are attributed to uncertainties in the precise densities of impurities.

IV. Plasma Properties with an Immersed Dielectric Droplet

Properties of the bulk plasma and the sheath surrounding the dielectric droplet are discussed in this section. The base case was an RF glow discharge operating at 10 MHz with 5 W power deposition. The plasma was sustained in He with 20 ppm of dry air impurity (16 ppm N_2 and 4 ppm O_2). The initially nonconductive 80 μm diameter dielectric droplet with $\varepsilon_r = 80$ was placed in the center of the plasma.

A. Bulk plasma properties

The bulk plasma properties averaged over one quasi-steady state RF cycle are shown in Figs. 5-8 for the base case (5 W) as well as the parameter sweeps discussed in the next two sections. The voltage amplitude to deliver 5 W was 326 V. (There is essentially no DC bias in this geometrically symmetric system.) The bulk electron density is 7.5×10^{11} cm^{-3} on the central axis several droplet diameters away from the droplet. At low power deposition (5 W being at the top of that range), the 80 μm diameter droplet influences the electron density across the width of the bulk plasma. The droplet produces a shadow of electron density on either side. The electric field in the bulk plasma a few diameters away from the droplet oscillates with an amplitude of about 80 V/cm or an E/N of 0.33 Td for which the drift velocity of electrons in pure He is 2.7×10^5 cm-s^{-1}. During ¼ of the 100 ns RF cycle, electrons drift about 35 μm, so at least a portion of the electron exclusion is due to physical shadowing or obscuration of the electrons' horizontal motion by the droplet. This effect is likely exaggerated by the 2D simulation, in which the droplet appears to be a rod, and so provides no avenue for electrons moving horizontally to avert the droplet at the axial location of the droplet (perpendicular to the computational domain). If the droplet was spherical, electrons drifting horizontally at the height of the droplet would have the option of drifting around the droplet.

The time-averaged E/N has a maximum value of 23 Td (5625 V/cm) in the sheaths that form at the electrodes. The instantaneous maximum is 51 Td (12,500 V/cm). The time-averaged E/N value in the bulk plasma is less than 0.25 Td (61 V/cm) with an instantaneous maximum of

0.35 Td (86 V/cm). The electron temperature T_e is largely determined by heating by the oscillating sheath at the electrodes and secondarily by joule heating in the bulk plasma. The time-averaged maximum T_e is 3.75 eV at the sheath edge at the electrodes with an instantaneous maximum of 6 eV. In the bulk plasma (on axis), the time-averaged T_e is 0.2 eV with instantaneous maximum of 0.3 eV. This range of T_e is similar to that reported in modeling by Liu et al [30]. The thickness of the sheath at the electrodes was 500 μm on a time-averaged basis.

Primary ionization and excitation of He is dominated by the sheath heated electrons within 300-400 μm of the electrodes. Ionization is dominated by Penning processes of He excited states and the air impurities in the bulk plasma where the net electron impact ionization source is negative. That is, the rate of direct electron impact ionization is lower than losses by dissociative recombination. The electron temperature is lower in the bulk plasma compared to, for example, the COST plasma jet due to the larger inter-electrode gap. With sheath heating dominating, plasmas having a smaller gap between the electrodes will have higher electron temperatures on axis [28,30–32].

Volume-averaged densities are shown in Fig. 9 as a function of time over the RF cycle. With the exception of He^+, the charged particle densities are nearly constant over the RF cycle. The electron density is 1.8×10^{11} cm^{-3} with N_2^+ and O_2^+ having densities near 1.4×10^{11} and 5.4×10^{10} cm^{-3}, respectively, being the dominant positive ions. While N_2 and O_2 have only impurity level densities, the ionization potentials of N_2 and O_2 are lower than that of He, leading to N_2^+ and O_2^+ becoming the dominant positive ions through charge exchange and Penning ionization processes. He_2^+ is the dominant helium ion, with a density near 10^9 cm^{-3}. The negative ions O_2^- and O^- are primarily formed by three-body and dissociative attachment to O_2, respectively, and have densities near 10^8 cm^{-3}. The density of He^+ oscillates between 3×10^7 cm^{-3} – 10^8 cm^{-3} over the RF cycle. This oscillation indicates He^+ is produced and consumed at different times during the RF cycle. In spite of the rate of formation of He^+ by electron impact at the sheath edge being the largest of all ions due to its large mole fraction, its rapid rate of dimerization to form He_2^+ and charge exchange with impurities rapidly depletes its density. Since T_e in and adjacent to the sheaths oscillates over the RF cycle, the production of He^+ also oscillates over the RF cycle.

Neutral radicals and excited states are shown in Figs. 9b and 9c during the RF cycle. The volume-averaged densities of metastable electronic states (e.g., $N_2(A)$, $O_2(^1\Delta)$, $O_2(^1\Sigma)$, $He(2^3S)$), vibrationally excited molecules, and radicals do not significantly oscillate over the RF cycle due

to their low rates of quenching and reaction. The excited states of He with shorter radiative lifetimes or trapped lifetimes have moderate oscillation.

B. Sheath Surrounding the Droplet

As an electrically floating body in the plasma, the droplet will acquire an electrical charge which, on a time-averaged basis, balances the currents of positive and negative species to the surface. In doing so, the surface of the droplet charges, and a sheath is formed at the surface of the droplet. In an electropositive plasma, the droplet should charge negatively compared to the local plasma potential to reflect a portion of the higher thermal flux of electrons compared to positive ions. In an isotropically uniform, quiescent plasma in which the electric field in the bulk plasma is small compared to the electric fields in the sheath, the surface charge on the droplet and sheath around the droplet should both be uniform. That is, a spherical or cylindrical droplet should have a sheath with a uniform thickness and sheath potential as a function of azimuthal position that is uniform.

The electron density, E/N, T_e, and charge density on the droplet are shown in Fig. 10 over the first half of a quasi-steady state RF cycle at 5 ns intervals in the 100 ns (10 MHz) period. (The second half of the RF cycle is not shown because the results mirror those of the first half.) The time-averages of these quantities over the RF cycle are shown in the last row of Fig. 10. A sheath forms around the droplet, indicated by the lower electron density and larger E/N in the vicinity of the droplet shown in Fig. 10a and 10b. The mean free path for electrons and ions at 1 atm is less than 2 μm, whereas the average thickness of the sheath is more than 100 μm resulting in the sheath being collisional. (Sheath thickness around the droplet is defined in this work as the location where the net charge density is 0.01 that of the positive ion density to capture where charge separation begins to occurs in the sheath. Since the gradient in charge density is steep at this location, our conclusions are not particularly sensitive to the precise value of charge density that designates the edge of the sheath.) The sheath is not circular and is elongated along the equator (in the horizontal direction) due, in part, to the influence of the applied horizontal electric field and the polarization of the droplet. During the RF cycle along the equator, the sheath thickness varies from 20 μm to 130 μm. At the poles (in the vertical direction), the sheath thickness varies from 70 μm to 90 μm. The Debye length in this system is 16.4 μm, which is typically smaller than the sheath thickness around the droplet based on the average charge. This is also consistent with the classic derivation of sheath thickness based on the Bohm criterion.

The properties of the sheath around the droplet, including the electron density, oscillate over the RF cycle out of phase with the sinusoidal applied voltage. The applied voltage to the powered electrode is maximum at 25 ns into the RF cycle which does not coincide with the maximum deformation in the sheath. The charging and discharging of the droplet can be viewed as that of a capacitor, and so the response of the droplet can be approximated as an RC circuit. The impedance of the RC circuit is complex due to the capacitor, leading to a phase difference ϕ between the voltage and the current. This phase angle is given by

$$\cos(\phi) = \frac{R}{\sqrt{R^2 + \left(\frac{1}{\omega C}\right)^2}}, \tag{3}$$

where R is the series resistance, ω is the radian frequency of the voltage oscillation, and C is the series capacitance. The series capacitance is due to the capacitance of the sheath at the electrode, the sheath around the droplet, and the droplet itself. The capacitance of the sheaths at the electrodes $C_{s,e}$ [34] in series with the droplet is

$$C_{s,e} = \frac{1.226\varepsilon_0 A}{\lambda_D}, \tag{4}$$

where ε_0 is the permittivity of free space, $A = \pi R_p^2$ is the cross-sectional area of the droplet with radius R_p, and λ_D is the Debye length, used as an estimate of sheath thickness. Note $C_{s,e}$ is the capacitance of the sheath at one electrode and must be accounted for twice in calculating the series capacitance of the system. The capacitance of the sheath around the droplet $C_{s,d}$ is approximately

$$C_{s,d} = \frac{4\pi\varepsilon_0}{\frac{1}{R_p} - \frac{1}{R_s}}, \tag{5}$$

where R_s is the radius of the sheath, estimated to be the semimajor axis of the elliptical sheath. The capacitance of the droplet C_d is

$$C_d = 4\pi\varepsilon_0\varepsilon_r R_p, \tag{6}$$

where ε_r is the relative permittivity of the droplet. Plasma resistance was calculated from the bulk plasma conductivity σ

$$\sigma = \frac{e^2 n_e}{m_e \nu_m}, \tag{7}$$

where e is the fundamental charge, n_e is the bulk electron density, m_e is the electron mass, and ν_m

is the momentum transfer collision frequency of electrons in the bulk plasma (3.5×10^{11} s^{-1}). From the conductivity, the resistance of the plasma was

$$R = \frac{L}{\sigma A}, \tag{8}$$

where L is the gap between the electrodes. With this analysis, the phase of the oscillation of the sheath was estimated to be 53°, closely matching the results of the model (54°).

In the absence of plasma, the polarization of the droplet by the horizontal external electric field produces a maximum in electric field at the surface of the droplet at the horizontal equator and a minimum at the axial poles. The polarization electric field outside a droplet of relative permittivity ε_r is

$$\vec{E} = E_0 \cos\theta \left[1 + 2\left(\frac{R_p}{r}\right)^3 \frac{\varepsilon_r - 1}{\varepsilon_r + 2}\right] \hat{a}_r - E_0 \sin\theta \left[1 - \left(\frac{R_p}{r}\right)^3 \frac{\varepsilon_r - 1}{\varepsilon_r + 2}\right] \hat{a}_\theta, \tag{9}$$

where θ is measured from the direction of the external electric field having magnitude E_o. The E/N in the vicinity of the droplet, Fig. 10b, results from the superposition of the electric field in the bulk plasma and the sheath electric field, modified by the polarization of the droplet. The electric field in the sheath surround the droplet is continuously directed inwards towards the droplet, while the electric field in the bulk plasma oscillates over the RF cycle. The superposition of these two electric fields enhances the total E/N at the equator on that side of the droplet (and phase in the RF cycle) that the sheath and bulk electric field both point in the same direction. The maximum of E/N near the droplet at the equator is 4 Td. The superposition of these two electric fields minimizes the total E/N at the equator on that side of the droplet (and phase in the RF cycle) that the sheath and bulk electric field point in opposite directions. This superposition produces a zero in E/N when the sheath and bulk electric fields are equal. With the bulk applied electric field having a purely horizontal orientation, and the electric field in the sheath being axially directed, there is no direct competition between the bulk and sheath electric fields at the poles. The sheath thickness at the poles therefore experiences less modulation during the RF cycle than at the equator.

There is some degree of shadowing of the electron drift motion by the droplet that contributes to the asymmetry in the sheath. In pure He, the drift velocity for E/N = 2 Td is about 10^6 cm/s, which during ¼ of the RF cycle produces drift distance of about 300 μm. This distance exceeds the diameter of the droplet. With virtually no axial component of the bulk electric field,

the droplet effectively shadows electron drift motion at the equator, a shadow that must be filled in by diffusion. This shadowing lowers the average electron density along the equator on the opposite side of the droplet, which then translates to a thicker sheath.

T_e over the RF cycle is shown in Fig. 10c in the vicinity of the droplet. T_e oscillates with the same phase as the electron density and E/N. The maximum in T_e near the droplet is 0.35 eV and occurs at about 45° above and below the horizontal plane. It is in this region that the power deposition per electron is the highest. It is also at this location that the polarization electric field is zero. However, the time-averaged maximum in T_e occurs at the poles. It is at these locations that the E/N is always finite and does not experience a zero-crossing. The time-averaged minimum in T_e occurs at the equator of the droplet as this is where the E/N is, on the average, lowest due to the canceling of bulk and sheath fields. While T_e does vary over the RF cycle near the droplet, the variation is small for these conditions (< 0.35 eV). Therefore, reactive species fluxes to the droplet will likely not vary based on the change in T_e near the droplet. The majority of reactive species are produced further away near the sheaths at the electrodes. That said, rotational and vibrationally excited species fluxes may change based on this small change in T_e.

The charge density on the droplet is shown in Fig. 10d. Since the droplet is nonconductive, and its charging time exceeds the RF period, the charge density on the surface does not significantly change over the RF cycle after coming into equilibrium following approximately 20 RF cycles or about 2 μs. With the droplet being a floating dielectric in an electropositive plasma, the total charge density on the particle must be negative, as it is here. The total average charge is $-1.5 \times 10^7 q$ (where $q = 1.6 \times 10^{-19}$ C), producing a time-averaged sheath potential of -1.5 V along the equator and -1.4 V along the poles, commensurate with the low time-averaged electron temperature.

The distribution of the charge on the droplet is non-uniform. The surface is charged negatively at the equator and is charged positively at the poles. This disparity in charging is due in part to the directed drift of electrons and due in part to the polarization electric fields. With there being shadowing of the electron drift motion by the droplet, the drift component of the electron flux into the sheath is smallest at the poles and largest at the equator. In fact, the decrease in horizontal electric field at the poles reduces the drift component. Electron transport to the sheath is dominated by drift at the equator while being dominated by diffusion to the poles. The ions, with lower mobility, largely respond to the time-averaged sheath electric field which transports

ions by drift to the surface of the particle throughout the RF cycle at all surface points. The lack of a drift component of electrons in the flux of the surface at the poles and dominance of the drift component of the electron flux at the equator leads to the differential charging. With there being no conductivity to redistribute these charges, an asymmetric charge distribution can be supported. This differential charging of the surface is allowed by the net charge on the droplet being negative, thereby placing the droplet, on the average, at a more negative potential with respect to the low plasma potential. The differential charging of the surface provides for the local changes in sheath potential that are required to balance electron and ion fluxes to that location.

The fluxes of the charged species to the droplet over the RF cycle are shown in Fig. 11. These results were extracted on the equator (left and right) and on the poles (top and bottom). Fluxes to the equator of the droplet are shown in Figs. 11a and 11b. With fluxes of electrons into the sheath being dominated by drift, the fluxes collected at the left and right equators are asymmetric and 180^{o} out of phase. Here, the polarization of the droplet produces large enough electric fields that even the ion fluxes have significant modulation. The maximum in ion flux coincides with a minimum in electron flux, which corresponds to that portion of the RF cycle that the opposing electric fields (sheath and bulk plasma) produce a maximum at the equator. The maximum in ion flux and minimum in electron flux are out of phase with the applied RF voltage, as shown in Fig. 11. The maximum of electron flux occurs at the minimum extension of the sheath when the electric fields in the sheath and bulk plasma oppose each other. At all locations, the peaks in the oscillation of all the fluxes were out of phase with the applied voltage and in phase with the oscillation of the sheath.

The fluxes of ions to the surface do not significantly vary over the RF cycle at the poles of the droplet, as shown in Figs. 11c and 11d. The flux of electrons is highly modulated over the RF cycle as the electrons with a higher mobility respond to the changing electric field more quickly than the ions. The flux of electrons to the poles peaks twice over the RF cycle at $2 - 4 \times 10^{15}$ cm^{-2} s^{-1}. Transport of electrons to the poles is dominated by axial diffusion which is not particularly sensitive to the direction of the horizontal electric field. However, the availability of electrons in the vicinity of the poles which are then available to diffuse to the poles is sensitive to the horizontal electric fields. Fluxes to the top and bottom poles are essentially the same.

V. Sheath Characteristics for Different Droplet Properties

A. Permittivity

With the droplet being an electrically floating body in the plasma, its charging and discharging during the RF cycle will be a function of its electrical permittivity, or its capacitance. The RF cycle averaged electron density, E/N, and T_e of the bulk plasma are shown in Figs. 5b, 6b, and 7b for ε_r = 1 to 80. The influence of the droplet on the plasma is in large part manifested by the exclusion of bulk plasma by the sheath around the droplet, and the charge accumulation (and discharging) during the RF cycle. The charging and discharging of the droplet during an RF cycle is approximately 1.1×10^6q for all permittivities, which is a small fraction of the electron inventory in the vicinity of the droplet. As a result, the capacitive nature of the droplet does not significantly affect the bulk plasma. The permittivity of the droplet does affect the time to charge the droplet (larger permittivity, larger RC time constant).

However, near the droplet, ε_r of the droplet does affect the sheath, the spatial distribution of charge on the droplet, and the local electron density. The time-averaged electron density and charge on the droplet for ε_r = 1 to 80 are shown in Fig. 12a. As ε_r increases, the eccentricity of the sheath increases. In particular, the sheath extends further along the equator as ε_r increases whereas there is little change in sheath properties at the poles. This extension in the sheath is attributable to the more intense polarization electric fields at the equator with increasing ε_r. With ε_r =1, there are no polarization electric fields to perturb the sheath. The disparity in the shape of the sheath is then fully attributable to the drift component of the electron flux in the horizontal direction and shadowing of electron flux.

The azimuthal charge density on the surface of the droplet is a function of ε_r. With ε_r = 1, the droplet is negatively charged at all azimuthal positions with the largest negative charge density being at the poles. With the absence of polarization electric fields at ε_r = 1, the shadowing of the drift flux in the horizontal direction produces, on the average, lower electron fluxes to the equator compared to the poles. The time-averaged sheath potential at the equator is -1.0 V and at the poles is -1.3 V. As ε_r increases to 4, the negative charge density at the equator increases in magnitude. With ε_r = 20, positive charge density emerges at the poles of the droplet and negative density intensifies at the equator, while the average charge density on the droplet remains negative. The time-averaged sheath potential at both the equator and poles is -1.5 V. This charging pattern is retained with ε_r = 80 with the magnitude of the charge density increasing by a factor of 4 relative

to $\varepsilon_r = 20$ to account for the larger capacitance of the droplet. The time-averaged sheath potential at the equator is -1.5 V and at the poles is -1.4 V.

The oscillation of the electron density a distance $2R_p$ from the center of the droplet along the left equator is shown in Fig. 12b for $\varepsilon_r = 1$ to 80. With an increase in ε_r, the electron density decreases, which is largely a consequence of the sheath being thicker with larger ε_r producing a smaller electron density near the surface. With the polarization electric field saturating for $\varepsilon_r >$ 10-20, the electron density is similar with $\varepsilon_r = 20$ and 80. The phase of the electron density oscillation is similar for all ε_r, ranging from 54° for $\varepsilon_r = 80$ to 58° for $\varepsilon_r = 1$. These results match the predicted phases of oscillation, which varied from 53° for $\varepsilon_r = 80$ to 59° for $\varepsilon_r = 1$. Since the phase of oscillation is similar for all ε_r, the capacitance of the droplet is not the dominant factor in determining the phase.

The dynamics of E/N over one quasi-steady state RF cycle as well as the time-averaged values are shown in Fig. 13 for $\varepsilon_r = 1$, 4, 20 and 80. With $\varepsilon_r = 1$, E/N is maximum at the poles of the droplet. In the absence of polarization electric fields, there is no decrease in the applied electric field at the poles. The electric fields and formation of sheaths at the poles are solely due to diffusion of electrons and positive ions from the bulk plasma. However, in the absence of polarization of the droplet, the E/N still has a zero at the equator when the sheath and applied electric fields oppose each other. The end result is that the time-averaged E/N is maximum at the poles, leading to an oblate shape.

The maximum instantaneous E/N occurs on the equator of the droplet for $\varepsilon_r = 4$. However, the maximum of the time-averaged E/N occurs at the poles due to the lack of competition between the sheath electric field and the bulk electric field. As ε_r increases to 20 and 80, the magnitude of E/N increases, and the maximum of the time-averaged E/N shifts to the equator due to the increased polarization of the droplet.

B. Diameter

The diameter of the droplet was decreased from 80 μm to 60 μm and 40 μm. The bulk electron density does not significantly vary with the diameter of the droplet except along the equator of the droplet, where the electron density increases as the diameter of the droplet decreases. This increase in electron density occurs because the cross-sectional area of the droplet decreases, allowing more electrons to move around instead of becoming obscured and shadowed by the

droplet. E/N and T_e in the bulk plasma also do not significantly change as a function of diameter of the droplet.

While the bulk plasma does not significantly change, sheath properties near the droplet do depend on the diameter of the droplet, as shown by the time-averaged values in in Fig. 14. The maximum E/N increases and E/N becomes more azimuthally symmetric as the diameter decreases. The polarization of the droplet is independent of diameter; however, the extent of the polarization electric field beyond the surface of the droplet scales with the size of the droplet. With the sheath thickness largely a function of the bulk plasma properties, and so relatively constant with diameter of the droplet, the polarization electric field for the smaller droplets produces a smaller perturbation. With the shadowing of the electron flux being less severe with smaller diameters of the droplet, there is less horizontal elongation of the sheath. The spatial dependence of T_e is qualitatively the same for all diameters. With the droplet size being commensurate (or smaller) than the sheath thickness, we expect some dependence of sheath properties on droplet size independent of polarization and RF electric fields. For example, the curvature of the sheath increases as the ratio of the sheath thickness to droplet size increases.

The charge density on the droplet also varies with diameter. With small droplet sizes where the polarization electric fields are less influential and shadowing less severe, the uniformity of the surface charging improves. The same trend occurs when varying the permittivity of the droplet. The charge distribution for $\varepsilon_r = 1$ and $\varepsilon_r = 4$ is more uniform due to the smaller influence of the polarization of the droplet by the plasma. The same process is occurring with smaller diameters.

C. Conductivity

The previous discussion addressed the sheath properties surrounding a nonconductive dielectric droplet. The conductivity of water can range from 5×10^{-8} S/cm (ultrapure water) to 5×10^{-2} S/cm (sea water). To examine how the conductivity of the droplet affects the sheath around the droplet, the conductivity of the dielectric droplet was varied from 0 to 10^{-1} S/cm. The bulk plasma properties (electron density, E/N, and T_e) do not significantly vary as the conductivity of the droplet was increased, as shown in Figs. 5c, 6c, and 7c. The charging and discharging of the droplet over the RF cycle is about 1.2×10^6q which is not enough to affect the bulk plasma.

Regardless of the conductivity of the droplet, the droplet is a floating electrical body in the plasma which, on a time-averaged basis, should collect no net charge. In this regard, the charging

potential, total charge, and sheath properties should not be a sensitive function of droplet conductivity. The time-averaged total charge on the droplet increases slightly from -1.5×10^7q on the nonconductive droplet to -1.9×10^7q for a droplet with a conductivity of 10^{-1} S/cm. However, the distribution of charge and how the droplet maintains the floating potential do depend on the droplet conductivity, as shown in Fig. 15. The charge density on the droplet is shown every 25 ns during the first 50 ns of the quasi-steady state RF cycle, along with the time-averaged values for droplet conductivities of $\sigma = 10^{-1}$, 10^{-5} and 10^{-7} S/cm. The charge density on the least conductive droplet, 10^{-7} S/cm, essentially does not oscillate over the RF cycle and has regions of positive and negative charge, as is the case for the nonconductive droplet. With an increase in conductivity to 10^{-5} S/cm and larger, there is a distinct change in the charge distribution to being uniformly negatively charged. The magnitude of the negative charge density at the poles of the of $\sigma = 10^{-5}$ S/cm droplet is 1 order of magnitude less than that at the equator, a remnant of the positive charging of less conductive droplets. The charge density still does not oscillate significantly over the RF cycle.

With an increase in conductivity to 10^{-3} S/cm, the droplet remains uniformly negatively charged while the charge density oscillates over the RF cycle, side-to-side on the equator. The oscillation in charge density increases as the conductivity increases to 10^{-1} S/cm, as shown in Fig. 15a. The higher conductivity is able to redistribute net positive charging at the poles produced with low conductivity to be an average surface charge over the entire droplet. With the net charge on the droplet being negative, this results in a negative surface charge over the entire droplet. With moderate conductivity, this redistribution occurs over many RF cycles. With the highest conductivity, this redistribution occurs in real time during a single RF cycle.

In traversing the plasma from electrode to electrode through the droplet, current continuity must be maintained. With the bulk plasma properties being a weak function of the droplet conductivity, the current flowing through the droplet should also be a weak function of conductivity. While the total current flowing through the droplet should not change with conductivity, the proportion of current that is displacement current and conduction current does change with conductivity. This change in character of the current is shown in Fig. 16, displaying the conduction and displacement current density at the center of the droplet over one quasi-steady state RF cycle. The current is entirely displacement current when the droplet is nonconductive. Displacement current dominates for conductivities up to 10^{-5} S/cm. As shown in Fig. 15, the charge density on the surface of the droplet does not oscillate over the RF cycle for this range of conductivity. For

droplet conductivities of 10^{-3} S/cm and higher, the conduction current is the same order of magnitude as the displacement current, as the conductivity is large enough to support charge transport through the center of the droplet. With a droplet conductivity of $\sigma = 10^{-1}$ S/cm, the conduction current through the droplet dominates over the displacement current. Although not calculated here as part of the simulation, the droplet may be heated by these conduction currents. For example, the power deposition at the center of the droplet is 40 μW cm^{-3}.

VI. Properties of the Plasma

The consequences of RF frequency and discharge power on droplet sheath properties were investigated.

A. RF Frequency

The time-averaged electron density, E/N, and T_e for the entire discharge are shown in Fig. 8 for RF frequencies of 10 MHz and 50 MHz while keeping the power constant at 5 W. Time-averaged values of electron density, E/N, T_e, and charge density near the droplet are shown in Fig. 17. The magnitude of the bulk electron density was similar between the two frequencies, as shown in Fig. 8. However, the sheath is more symmetric at the higher frequency. While the ions do not significantly drift during the RF period for either frequency, electrons do significantly drift over half the RF cycle. That distance is approximately 30 μm at 50 MHz and 300 μm at 10 MHz. The former is commensurate with the diameter of the droplet whereas the latter is larger than the droplet diameter. This drift distance is 10 times lower at 50 MHz than at 10 MHz due both to the shorter period and the lower bulk electric field resulting from the lower applied voltage – 159 V at 50 MHz and 326 V at 10 MHz. The end result is that there is little shadowing of the electron flux by the droplet at 50 MHz while having significant shadowing by the droplet at 10 MHz. The greater shadowing at the lower frequency produces a more asymmetric sheath.

The asymmetry in the sheath surrounding the droplet at 50 MHz is largely due to the polarization of the droplet and less due to shadowing of the electron flux. The time-averaged sheath potential at 50 MHz (-5.4 V at the equator and -3.7 V at the poles) is at least 2.5 times larger than at 10 MHz (-1.5 V at the equator and -1.4 V at the poles) which then produces commensurate increases in E/N in the sheaths. These differences largely account for the increase in T_e surrounding the droplet that occurs at 50 MHz (0.65 eV) compared to 10 MHz (0.23 eV). T_e is also more uniformly distributed around the droplet at the higher frequency.

The distribution of charge density on the surface of the droplet does not significantly depend on RF frequency, as the poles are positively charged and the equator is negatively charged at both frequencies. However, at 50 MHz, the magnitudes of the positive and negative charges are at least three times higher than at 10 MHz, a consequence of the higher bulk T_e. Given that the charge distribution is nearly independent of frequency while shadowing is sensitive to frequency, the bipolar charge distribution is largely attributable to polarization of the droplet.

The oscillation of the electron density at $2R_p$ from the center of the droplet along the left equator and the top pole is shown in Fig. 18a over one RF cycle for frequencies of 10 MHz and 50 MHz. While the electron densities at the equator are commensurate at 10 MHz and 50 MHz, the electron density at the pole is almost 3 times larger at 10 MHz than 50 MHz. The electron density is higher at 10 MHz because the sheath is more asymmetric, being thinner at the pole than along the equator due to the dominance of shadowing. The electron density at $2R_p$ from the center of the droplet is then more reflective of the bulk plasma density. The phase of the electron density oscillation at 50 MHz, -1.8°, is nearly in phase with the applied voltage. The dynamics of E/N are shown in Fig. 18b at 5% of a diameter away from the left equator and from the top pole of the droplet. At the poles of the droplet, E/N does not oscillate significantly, with E/N twice as large at 50 MHz (4.1 Td) than at 10 MHz (2.1 Td) due to the lack of drift current directed into the poles. The same relative increase in E/N occurs at the equator where there is significant oscillation - 1.5 Td at 10 MHz and 3.5 Td at 50 MHz.

B. Power Deposition

The time-averaged electron density, E/N, and T_e for the entire discharge are shown in Figs. 5a, 6a, and 7a, for power deposition of 1, 5, 10 and 15 W. With the increase in power deposition, the plasma transitions from the α-mode (dominated by bulk ionization) to the γ-mode or Penning mode (dominated by sheath ionization). The α-mode has the highest electron density in the bulk plasma, while the γ-mode has the highest electron density near the sheath edge [28,29]. The time-averaged bulk electron density at 1 W is 1.4×10^{11} cm^{-3} (applied voltage amplitude 235 V) and 7.7×10^{11} cm^{-3} at 5 W (326 V), both operating in α-mode. At 10 W (278 V), the electron density in the bulk plasma increases to 9.9×10^{11} cm^{-3} while the maximum shifts to the sheath edge at 1.5×10^{12} cm^{-3}, indicative of the start of the γ-mode or Penning mode. The bulk and sheath edge electron densities are 3.8×10^{11} cm^{-3} and 1.3×10^{12} cm^{-3} at 15 W (355 V). This voltage decrease

is characteristic of the transition between the α- and γ- modes [28,29]. While the maximum time-averaged E/N occurs in the sheaths near the electrodes at all powers, as shown in Fig. 6a, the maximum time-averaged E/N increases from 1 W (7 Td) to 10 W (30 Td) and slightly decreases at 15 W (29 Td). Similar to E/N, the maximum T_e occurs at the sheath edges, with cycle averaged T_e in the bulk plasma decreasing from 0.3 eV at 1 W to 0.16 eV at 5 W and increasing to 0.22 eV at 10 W and 1 eV at 15 W. The maximum T_e in the bulk plasma increases from 0.4 eV at 1 W to 1.7 eV at 15 W.

Since the electron density and T_e vary as a function of power, the relative abundances of ions and excited states change as well. The volume-averaged densities ions as a function of power are shown in Fig. 19. To compare ion composition between powers, these densities are normalized to the volume-averaged electron density at each power. The normalized densities of N_2^+ and O_2^+ do not significantly change as a function of power. Charge exchange reactions are rapid enough that helium monomer and dimer ions are consumed by reactions with the impurities at all powers. The relative density of O_2^- decreases with increasing power as the rate coefficient for three-body attachment to O_2 is proportional to T_e^{-2}, thereby decreasing its rate of formation as electron temperature increases with power. Although T_e increases with power, the rate of formation of O^- by dissociative attachment is low at all powers. The relative density of O^- decreases in large part because the rate of ion-ion neutralization increases with power. The relative densities of He^+ and He_2^+ increase with power in large part due to the increase in T_e.

The time-averaged sheath properties near the droplet are shown in Fig. 20 for powers from 1 – 15 W. With the increase in bulk plasma density, the sheath thickness decreases from 1 W to 10 W, and the sheath becomes more symmetric. However, at 15 W, the sheath again becomes asymmetric due to shadowing by the increasing contribution of drift current. The maximum of the time-averaged E/N occurs at the equator of the droplet for all powers with the symmetry improving from 1-10 W and becoming asymmetric at 15 W. The pattern of droplet charging is the same at all powers, negative at the equator and positive at the poles.

VII. Concluding Remarks

An important aspect of plasma-liquid interactions and the plasma-activation of liquids is the sheath that forms at the liquid surface. This is particularly important in plasma activation of droplets due to their high surface-to-volume ratio. In this study, the properties of sheaths around

droplets immersed in an atmospheric pressure RF He plasma with air impurities were investigated using a 2D model. The droplet was modeled as being a dielectric to isolate the electrical properties of the plasma-droplet interactions from those resulting from chemistry. The reactor conditions were an electrode separation of 3 mm, length of 9.5 mm with power deposition of 1-15 W at a frequency of 10 MHz or 50 MHz. Droplet diameters of 40-80 μm, relative permittivities of 1-80, and conductivities up to 0.1 S/cm were investigated.

For most of the conditions investigated, the sheath surrounding the droplet was asymmetric, elongated in the horizonal direction aligned with the applied electric field. This asymmetry results from polarization of the droplet that maximizes the electric field on the equator of the droplet and shadowing of the horizontal drift motion of electrons due to the bulk electric field. With the charge on the droplet and bulk plasma properties being in a quasi-steady state during the RF cycle for most conditions, the sheath forming at the surface of the droplet should be symmetric, producing electric fields pointing radially inward towards the droplet. However, both the polarization electric field produced by the droplet and the bulk electric field alternate in direction and magnitude every half-cycle and are largest in the horizontal direction. The vector sum of the *natural* sheath electric field and the bulk electric field produces maxima and minima in the total electric field on opposite sides of the droplet along the equator. The end result is oscillation in the extent of the sheath at the equator. Since the bulk electric field is purely horizontal, there is less modulation of the sheath electric fields and less modulation in the sheath's extent at the poles of the droplet. The polarization dynamics in the sheath thickness scale with the permittivity of the droplet while being less a function of the discharge conditions.

The drift and shadowing component of the sheath asymmetry is more sensitive to plasma conditions. In He, the electron drift velocity is high enough that during a 10 MHz cycle, the electrons can drift more than the diameter of the droplet. This drift increases the electron density on one side of the droplet, thinning the sheath at the equator, and decreases electron density on the other side of the droplet, extending the sheath at the equator. Since the bulk drift current does not flow directly into the poles of the droplet, charged particle fluxes into the poles are diffusion dominated with thickness that is only weakly modulated during the RF cycle. Molecular gas mixtures having lower electron mobilities and lower drift velocities will produce less shadowing by the droplet and less modulation in the sheath properties. Operating at higher frequencies will reduce the drift contribution to the sheath asymmetry.

With the droplets being electrically floating bodies in an electropositive plasma, the droplets charge, on the average, negatively and acquire, on the average, a negative potential with respect to the local plasma potential. The net negative charge on the droplets occurred for all conditions examined. That said, the distribution of charge on the droplets is not necessarily uniform. For what may be ideal conditions – no rotation of the droplet, no photo-electron emission, negligible conductivity – the droplets generally charged positive at the poles and negative at the equator while the total charge was negative. With charged particle fluxes being diffusion dominated at the poles while electron fluxes at the equator are drift dominated, there is an excess of electron charge collected at the equator. The response of the sheaths is to flatten at the poles, letting through an excess of positive charge, to retain its needed droplet averaged charge balance. With the droplet not rotating, this is a quasi-steady state configuration. With a sufficiently high droplet conductivity, the charge distribution on the droplet becomes more uniform, becoming negative at the poles.

Conductivity of the droplet also affects the manner in which current continuity is maintained through the droplet. In most cases, the droplet has little effect on the bulk plasma properties beyond the extent of the sheath. For low conductivities, current continuity is maintained by displacement current through the droplet. While the total current through the droplet does not significantly change when increasing the conductivity of the droplet, conduction current through the droplet increases, and eventually dominates at a conductivity of 10^{-1} S/cm.

We stated that changes in droplet properties do not greatly affect the bulk plasma properties. However, the bulk plasma properties with-and-without the droplet can be affected. The plasma density at the height of the droplet was generally lower than above and below the droplet. This decrease in plasma density is largely attributed to the shadowing of the electron drift motion by the droplet. The results discussed here were produced with a 2-dimensional model of a single, stationary droplet. This modeling method and choice of conditions were likely a worst-case scenario with respect to this local reduction in plasma density. The droplet appeared to be a rod and not a sphere. In 3-dimensions, the plasma can flow around the droplet, and if the droplet moves, its shadowing is averaged over space. Our results are, however, indicative of the long-range influence that larger droplets (tens of microns) can have on the plasma.

If plasma activation of a water droplet is dominated by fluxes of neutral radicals produced far from the droplet, these sheath dynamics may not have a large effect on that activation. However, droplet activation depending dominantly on charged particles fluxes (e.g., electron solvation)

will likely be sensitive to the sheath dynamics. The net positive charging at the poles of the droplet may result in a different ion chemistry than at the equator. Although these simulations were performed for a single, non-moving droplet, one can speculate on the consequences of the asymmetric sheath dynamics on a high density of droplets or for a distribution of droplet sizes. For droplet spacings commensurate with the sheath thickness, we might expect some non-ideal behavior even at atmospheric pressure, perhaps leading to a weak form of the Coulomb liquids produced at low pressures. Given that the sheath dynamics are asymmetric, equator vs pole, one may also expect some degree of anisotropy in the properties of the Coulomb liquids that might occur at high densities of droplets. For example, the spacing of the droplets in the Coulomb liquid in the horizontal direction in which the sheath is most elongated would likely be larger than in the axial direction in which the width of the sheath is typically smaller. Since the sheath properties and thickness are functions of the size of the droplets, a distribution of droplet sizes would likely lead to some additional disorder in the Coulomb liquid.

Our study focused on an electropositive plasma with only a small fraction of negative ions, about 10^{-3}. The negative ions had a negligible effect on the sheath properties. Based on prior studies of sheath properties in electronegative plasmas, we expect the trends discussed here for sheath properties around a droplet would apply to fairly large electronegativities as long as the electron temperature is high compared to the ion temperature. The sheath properties around the droplet in an afterglow where the electron temperature has thermalized would likely be more sensitive to negative ions.

Acknowledgements

This work was supported by the National Science Foundation (Nos. PHY-1902878, IIP-1747739 and PHY 1903151). This material was also based upon work supported by the U.S. Department of Energy, Office of Science, Office of Fusion Energy Sciences under Award No. DE-SC0020232; the Army Research Office accomplished under Grants Nos. W911NF-20-1-0105 and W911NF-18-1-0240).

Conflict of Interest

The authors have no conflicts of interest to disclose.

Data Availability

The data that support the findings of this study are available from the corresponding author upon reasonable request.

References

[1] P. F. Ambrico, M. Šimek, C. Rotolo, M. Morano, A. Minafra, M. Ambrico, S. Pollastro, D. Gerin, F. Faretra and R. M. De Miccolis Angelini, Sci. Rep. **10,** 3673 (2020).

[2] Y. He, C. Ding, T. Jin, Y. Fan, Z. Wu, M. Sun, K. Wang and T. Ji, Plasma Sci. Technol. **22,** 065502 (2020).

[3] J. E. Foster, S. Mujovic, J. Groele and I. M. Blankson, J. Phys. D. Appl. Phys. **51,** 293001 (2018).

[4] T. Von Woedtke, D. Weltmann, S. Emmert, H. Metelmann, S. Rupf and K.-D. Weltmann, Phys. Plasmas **27,** 070601 (2020).

[5] E. Casado, M. C. Garcia, D. A. Krawczyk, F. J. Romero-Salguero and A. Rodero, Plasma Process. Polym. **17,** 2000030 (2020).

[6] M. C. García, M. Mora, D. Esquivel, J. E. Foster, A. Rodero, C. Jiménez-Sanchidrián and F. J. Romero-Salguero, Chemosphere **180,** 239 (2017).

[7] F. Prehn, E. Timmermann, M. Kettlitz, K. Schaufler, S. Günther and V. Hahn, Plasma Process. Polym. **17,** 2000027 (2020).

[8] M. K. J. Nicol, T. R. Brubaker, B. J. Honish, A. N. Simmons, A. Kazemi, M. A. Geissel, C. T. Whalen, C. A. Siedlecki, S. G. Bilén, S. D. Knecht and G. S. Kirimanjeswara, Sci. Rep. **10,** 3066 (2020).

[9] C. Jiang, E. B. Sözer, S. Song, N. Lai, P. T. Vernier and S. Guo, Phys. Plasmas **27,** 113513 (2020).

[10] P. Heirman, W. Van Boxem and A. Bogaerts, Phys. Chem. Chem. Phys. **21,** 12881 (2019).

[11] N. C. Roy, C. Pattyn, A. Remy, N. Maira and F. Reniers, Plasma Process. Polym. **18,** 202000087 (2021).

[12] Y. Zheng, L. Wang and P. Bruggeman, J. Vac. Sci. Technol. A **38,** 063005 (2020).

[13] N. Akiyama, Y. Nakagawa, S. Uchida and F. Tochikubo, J. Appl. Phys. **129,** 163304 (2021).

[14] Z. Liu, S. Wang, B. Pang, H. Zhang, Y. Gao, D. Xu and M. G. Kong, J. Phys. D. Appl. Phys. **54,** 215203 (2021).

[15] M. E. Hassan, M. Janda and Z. Machala, Water **13,** 182 (2021).

[16] H. E. Delgado, G. H. Brown, D. M. Bartels, P. Rumbach and D. B. Go, J. Appl. Phys. **129,** 083303 (2021).

[17] J. A. Silsby, S. Simon, J. L. Walsh and M. I. Hasan, Plasma Chem. Plasma Process. **41,** 1363 (2021).

[18] G. Nayak, N. Sadeghi and P. J. Bruggeman, Plasma Sources Sci. Technol. **28,** 125006 (2019).

[19] G. Nayak, M. S. Simeni, J. Rosato, N. Sadeghi and P. J. Bruggeman, J. Appl. Phys. **128,**

243302 (2020).

[20] G. Oinuma, G. Nayak, Y. Du and P. J. Bruggeman, Plasma Sci. Technol. **29,** 095002 (2020).

[21] G. Nayak, G. Oinuma, Y. Yue, J. S. Sousa and P. J. Bruggeman, Plasma Sources Sci. Technol. **30,** (2021).

[22] S. A. Norberg, E. Johnsen and M. J. Kushner, Plasma Sources Sci. Technol. **24,** 035026 (2015).

[23] D. L. Scharfetter and H. K. Gummel, IEEE Trans. Electron Devices **16,** 64 (1969).

[24] W. Van Gaens and A. Bogaerts, J. Phys. D. Appl. Phys. **46,** 275201 (2014).

[25] S. Norberg, "Modeling atmospheric pressure plasma jets: Plasma dynamics, interaction with dielectric surfaces, liquid layers, and cells," Ph.D. thesis (University of Michigan, 2015).

[26] F. Emmert, H. H. Angermann, R. Dux and H. Langhoff, J. Phys. D. Appl. Phys. **21,** 667 (1988).

[27] A. M. Lietz, E. V Barnat, J. E. Foster and M. J. Kushner, J. Appl. Phys. **128,** 083301 (2020).

[28] J. Shi and M. G. Kong, IEEE Trans. Plasma Sci. **33,** 624 (2005).

[29] J. J. Shi and M. G. Kong, J. Appl. Phys. **97,** 1 (2005).

[30] D. X. Liu, J. F. Li, A. J. Yang, X. H. Wang, M. Z. Rong and M. G. Kong, High Volt. **1,** 81 (2016).

[31] D. X. Liu, A. J. Yang, X. H. Wang, M. Z. Rong, F. Iza and M. G. Kong, J. Phys. D. Appl. Phys. **45,** (2012).

[32] N. Balcon, G. J. M. Hagelaar and J. P. Boeuf, IEEE Trans. Plasma Sci. **36,** 2782 (2008).

[33] Phelps database, www.lxcat.net, retrieved on August 16, 2021.

[34] M. A. Lieberman, IEEE Trans. Plasma Sci. **16,** 638 (1988).

Table 1 – Species Include in the Model.

Charged Species	e, OH^-, H_2O^+, H_3O^+, O_2^+, O_2^-, O^+, O^-, N_2^+, N^+, $H_4O_2^+$, $H_2O_3^+$, $H_5O_2^+$, He^+, He_2^+
Neutral Species	H, H_2, OH, H_2O, HO_2, H_2O_2, O_2, O, N_2, N, He
Excited States	$H_2O(v)$, $O_2(v)$, $O_2(r)$, $O_2(^1\Delta_g)$, $O_2(^1\Sigma_u)$, $O(^1D)$, $N_2(r)$, $N_2(v)$, $N_2(A^3\Sigma_u)$, $N_2(a'^1\Sigma)$, $N(^2D)$, $He(2^3S)$, $He(2^1S)$, $He(2^3P)$, $He(2^1P)$, He(3P), He(3S), He_2^*

He_2^* is a lumped state of all He excited dimers.

Figure Captions

1. Geometry and numerical meshes used in the model. (a) Geometry and (b) numerical mesh to compare the simulated plasma properties to experimental plasma properties. (c) Geometry and numerical mesh to examine sheath properties around the droplet.
2. Numerical mesh near the droplet for diameters of (a) 40 μm, (b) 60 μm and (c) 80 μm.
3. Plasma properties for the He RF discharge. (a) Time-averaged bulk plasma properties (electron density, E/N, T_e) over one quasi-steady state RF cycle. (b) T_e across the plasma gap at various times during the RF cycle.
4. Comparison of model predictions to experimental measurements. (a) Emissivity fitted by Nayak et al [19](red) and emissivity calculated using model results (blue). (b) He metastable densities time-averaged over one quasi-steady state RF cycle extracted perpendicular to the electrodes and at the center of the electrode height. Model results (solid), and experimental measurements (points) for He(2^3S) (blue) and He_2^* (green).
5. Electron density averaged over one quasi-steady state RF cycle. (a) 1 W – 15 W, (b) droplet permittivity of $\varepsilon_r = 1$ to $\varepsilon_r = 80$, and (c) droplet conductivity of 10^{-7} – 10^{-1} S/cm.
6. E/N averaged over one quasi-steady state RF cycle. (a) 1 W – 15 W, (b) droplet permittivity of $\varepsilon_r = 1$ to $\varepsilon_r = 80$, and (c) droplet conductivity of 10^{-7} – 10^{-1} S/cm.
7. T_e averaged over one quasi-steady state RF cycle. (a) 1 W – 15 W, (b) droplet permittivity of $\varepsilon_r = 1$ to $\varepsilon_r = 80$, and (c) droplet conductivity of 10^{-7} – 10^{-1} S/cm.
8. Electron density, E/N, and T_e averaged over one quasi-steady state RF cycle for (a) 10 MHz and (b) 50 MHz.
9. Volume-averaged species densities for the base case over one quasi-steady state RF cycle. (a) Charged species, (b) neutral species, and (c) neutral species with densities that oscillate over the RF cycle.
10. Properties of the sheath near the droplet over half of one quasi-steady state RF cycle at 10 MHz (0 – 50 ns). (a) Electron density, (b) E/N, (c) T_e, and (d) charge density on the droplet. The last row shows the time-average of these quantities over one quasi-steady state RF cycle.
11. Flux of charged species to the (a) left equator, (b) right equator, (c) top pole, and (d) bottom pole of the droplet over one quasi-steady state 10 MHz RF cycle. Dashed lines show the maximum and minimum in the applied RF voltage.
12. Sheath properties for droplet permittivities of $\varepsilon_r = 1$ to $\varepsilon_r = 80$. (a) Time-averaged electron

density and charge density on the droplet over one quasi-steady state RF cycle. (b) Electron density at $2R_p$ from center of droplet along left equator of the droplet over one quasi-steady state RF cycle.

13. E/N over half of one quasi-steady state 10 MHz RF cycle (0 – 50 ns) for different permittivities of the droplet. The last row shows the time-average of E/N over the RF cycle. (a) ε_r =1, (b) ε_r = 4, (c) ε_r = 20, and (d) ε_r = 80.
14. Time-averaged electron density, E/N, T_e, and charge density on the droplet over one quasi-steady state 10 MHz RF cycle for different diameters of the droplet. (a) 40 μm, (b) 60 μm, and (c) 80 μm.
15. Charge density on the droplet over half of one quasi-steady state 10 MHz RF cycle (0 – 50 ns) for different conductivities of the droplet. The last row shows the time-average of these quantities over the RF cycle. (a) 10^{-1} S/cm, (b) 10^{-5} S/cm, and (c) 10^{-7} S/cm.
16. Current contributions through the center of the droplet for droplet conductivities of 10^{-1} S/cm, 10^{-3} S/cm, 10^{-5} S/cm, 10^{-7} S/cm, and a nonconductive droplet over one quasi-steady state RF cycle. (a) Displacement current density and (b) conduction current density.
17. Time-averaged electron density, E/N, T_e, and charge density on the droplet over one quasi-steady state RF cycle for frequencies of (a) 10 MHz and (b) 50 MHz.
18. Sheath properties for RF frequencies of 10 MHz and 50 MHz over one quasi-steady state RF cycle. (a) Electron density at $2R_p$ from the center of the droplet and (b) E/N at 5% of a diameter away from left equator (solid) and top pole (dashed).
19. Volume-averaged charged species densities over one quasi-steady state RF cycle as function of discharge power. Densities normalized to volume-averaged electron density.
20. Time-averaged electron density, E/N, T_e, and charge density on the droplet over one quasi-steady state RF cycle for discharge powers of 1 W to 15 W.

Journal of Applied Physics

AIP Publishing

Journal of Applied Physics

ACCEPTED MANUSCRIPT

PLEASE CITE THIS ARTICLE AS DOI: 10.1063/5.0103446

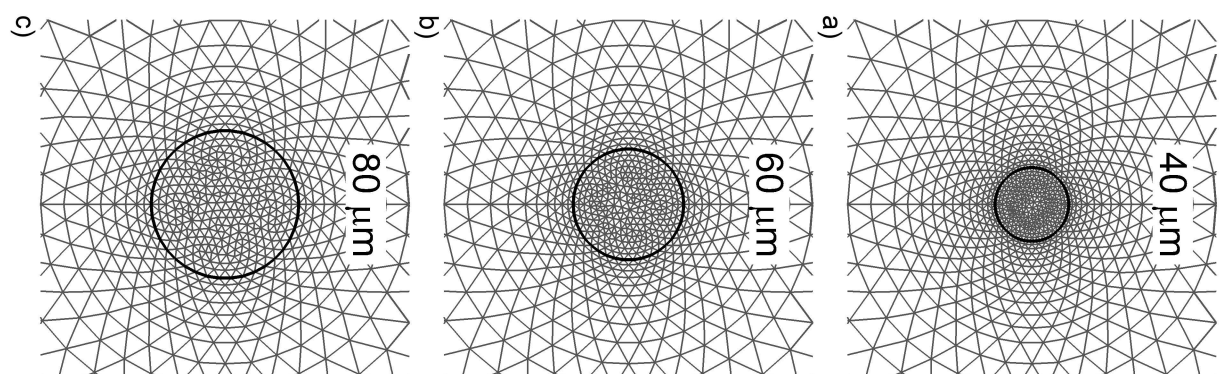

AIP Publishing

Journal of Applied Physics

ACCEPTED MANUSCRIPT

PLEASE CITE THIS ARTICLE AS DOI: 10.1063/5.0103446

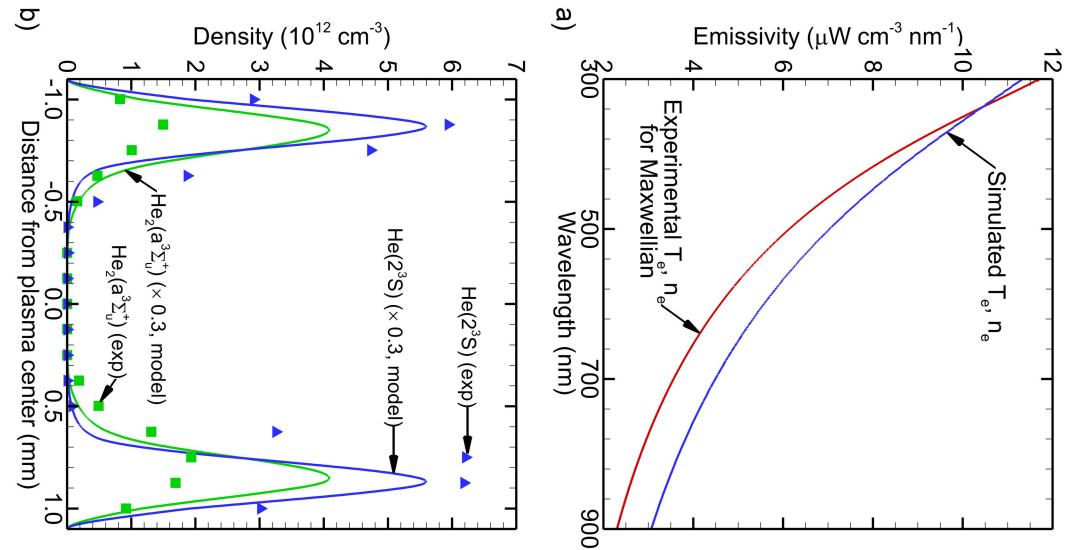

AIP Publishing

Journal of Applied Physics

PLEASE CITE THIS ARTICLE AS DOI: 10.1063/5.0103446

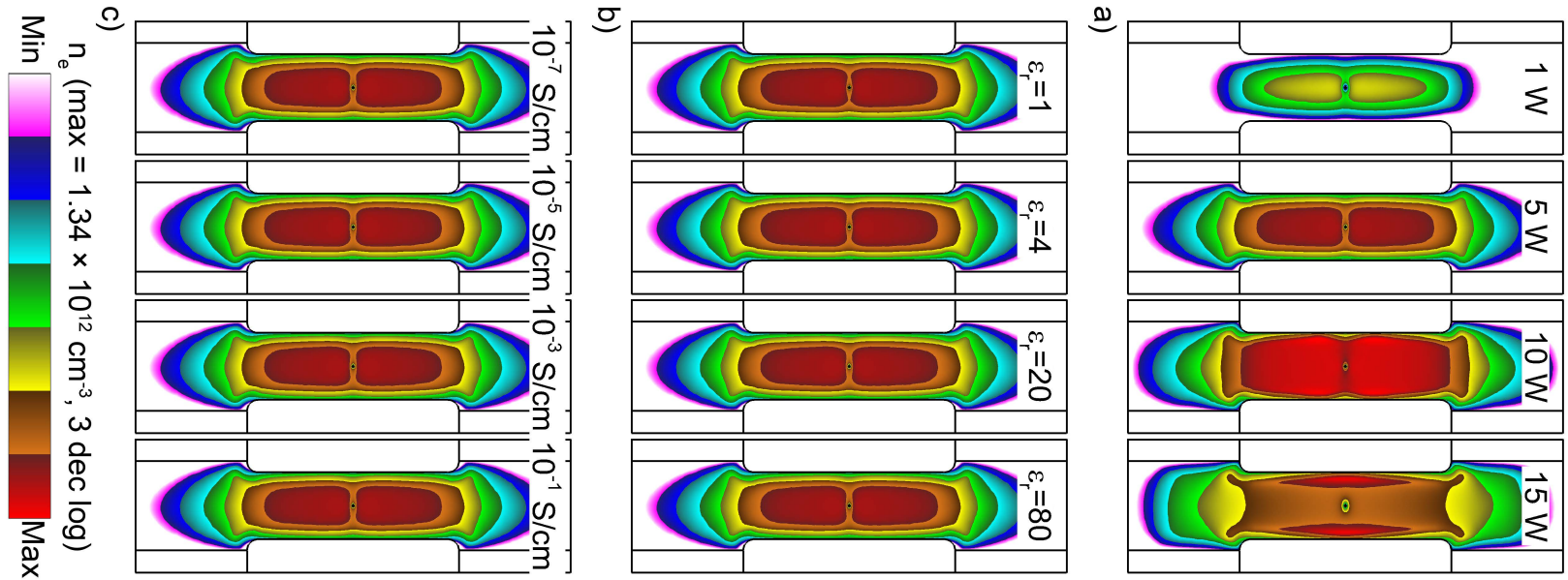

AIP Publishing

Journal of Applied Physics

ACCEPTED MANUSCRIPT

PLEASE CITE THIS ARTICLE AS DOI: 10.1063/5.0103446

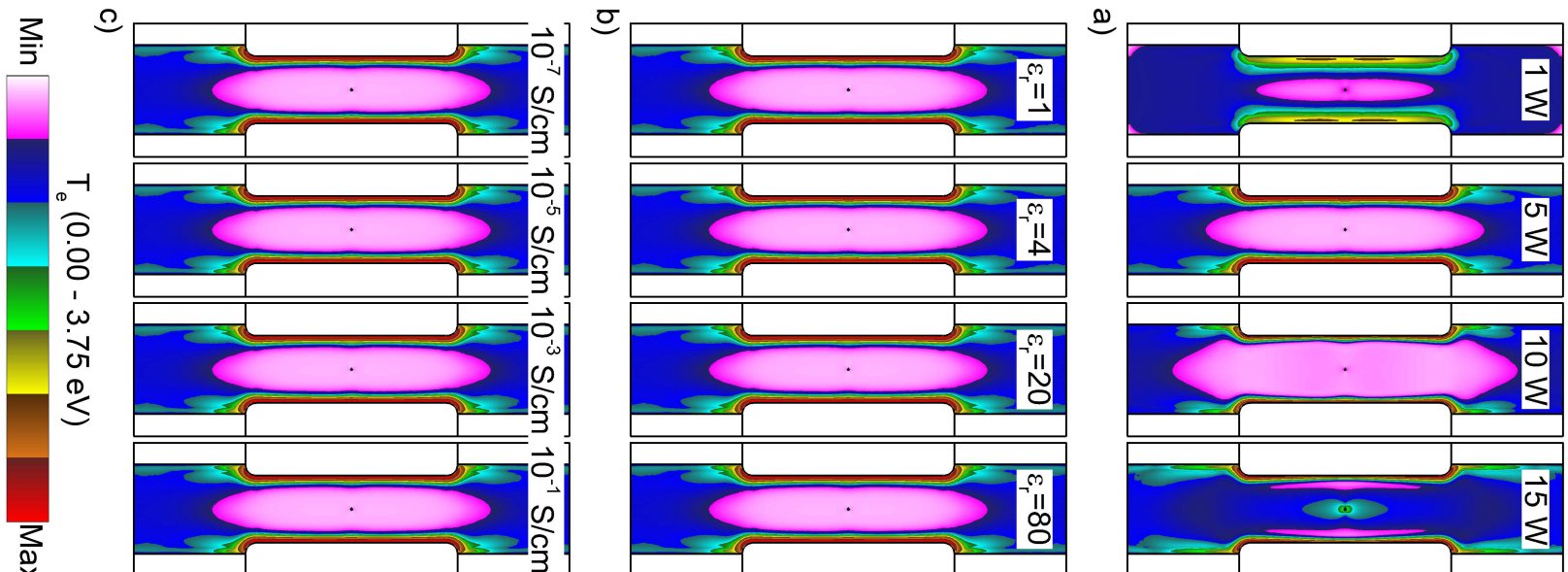

AIP Publishing

Journal of Applied Physics

ACCEPTED MANUSCRIPT

This is the author's peer reviewed, accepted manuscript. However, the online version of record will be different from this version once it has been copyedited and typeset.
PLEASE CITE THIS ARTICLE AS DOI: 10.1063/5.0103446

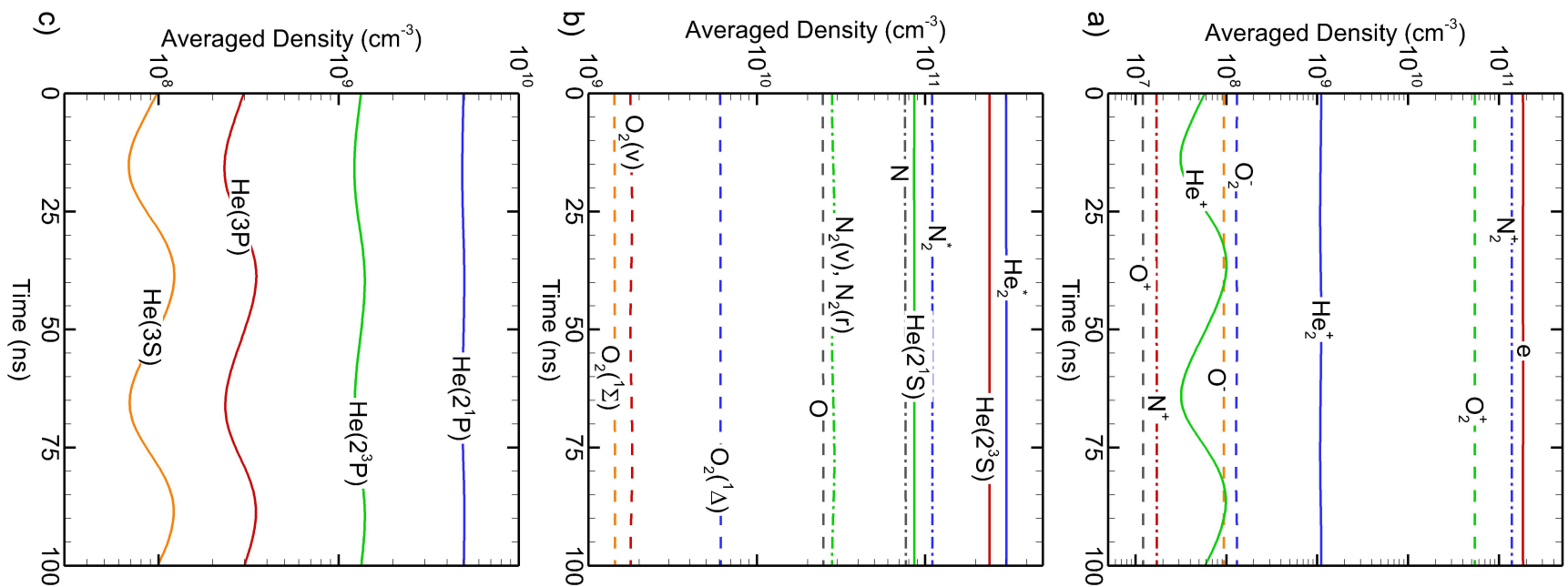

Journal of Applied Physics

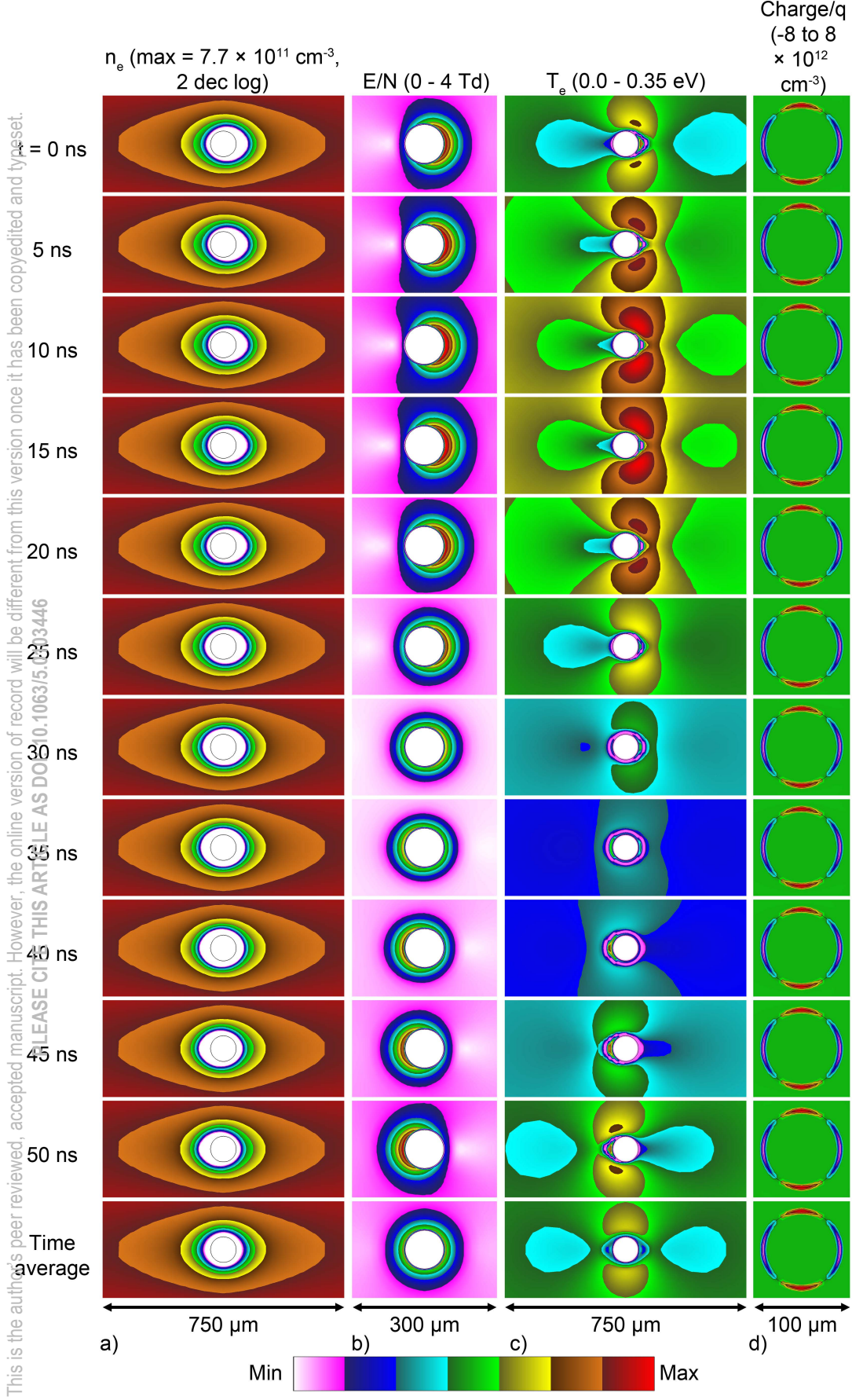

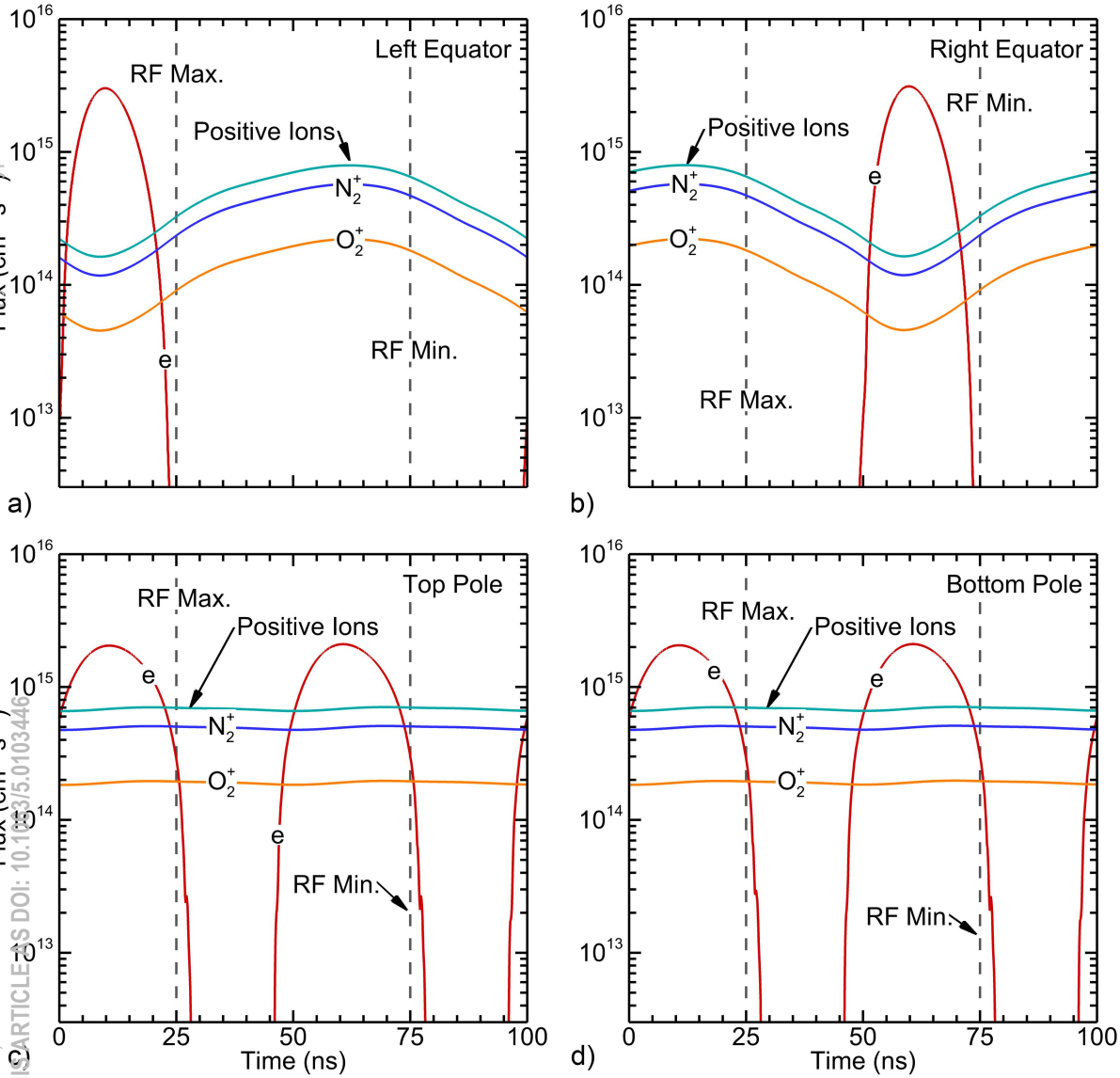

Journal of Applied Physics

AIP Publishing

Journal of Applied Physics

PLEASE CITE THIS ARTICLE AS DOI: 10.1063/5.0103446

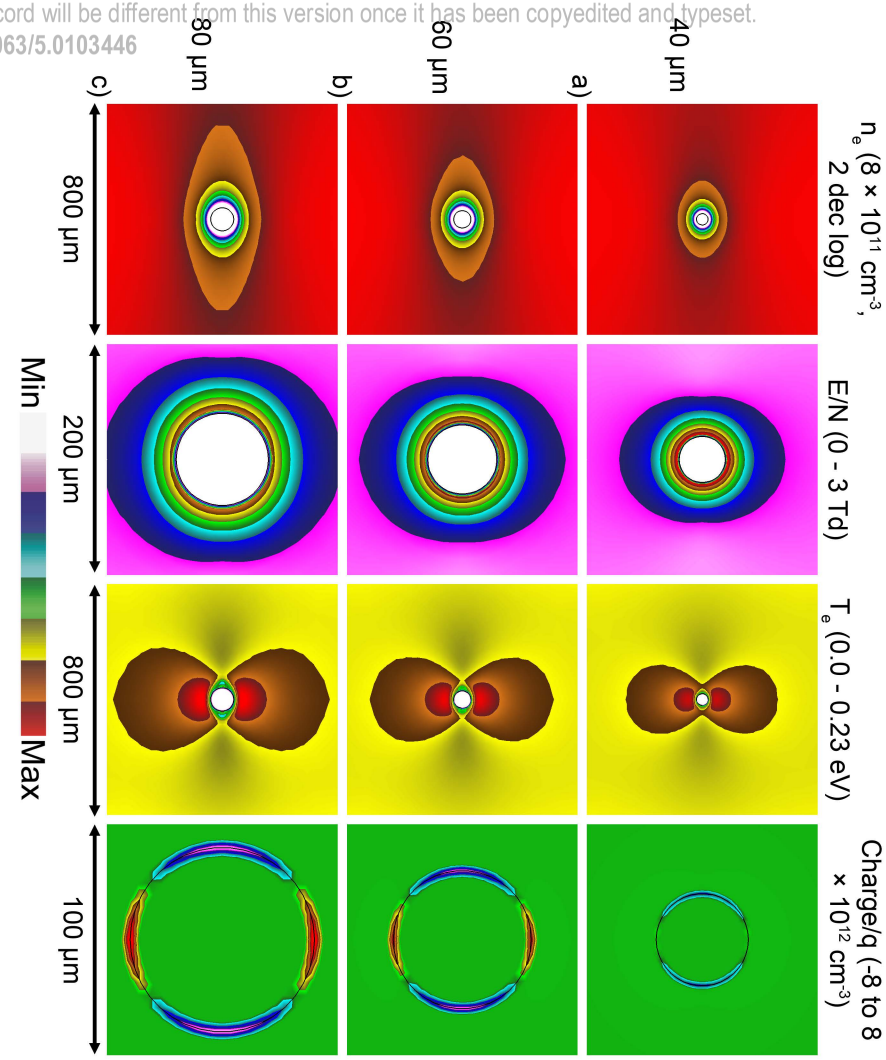

Journal of Applied Physics

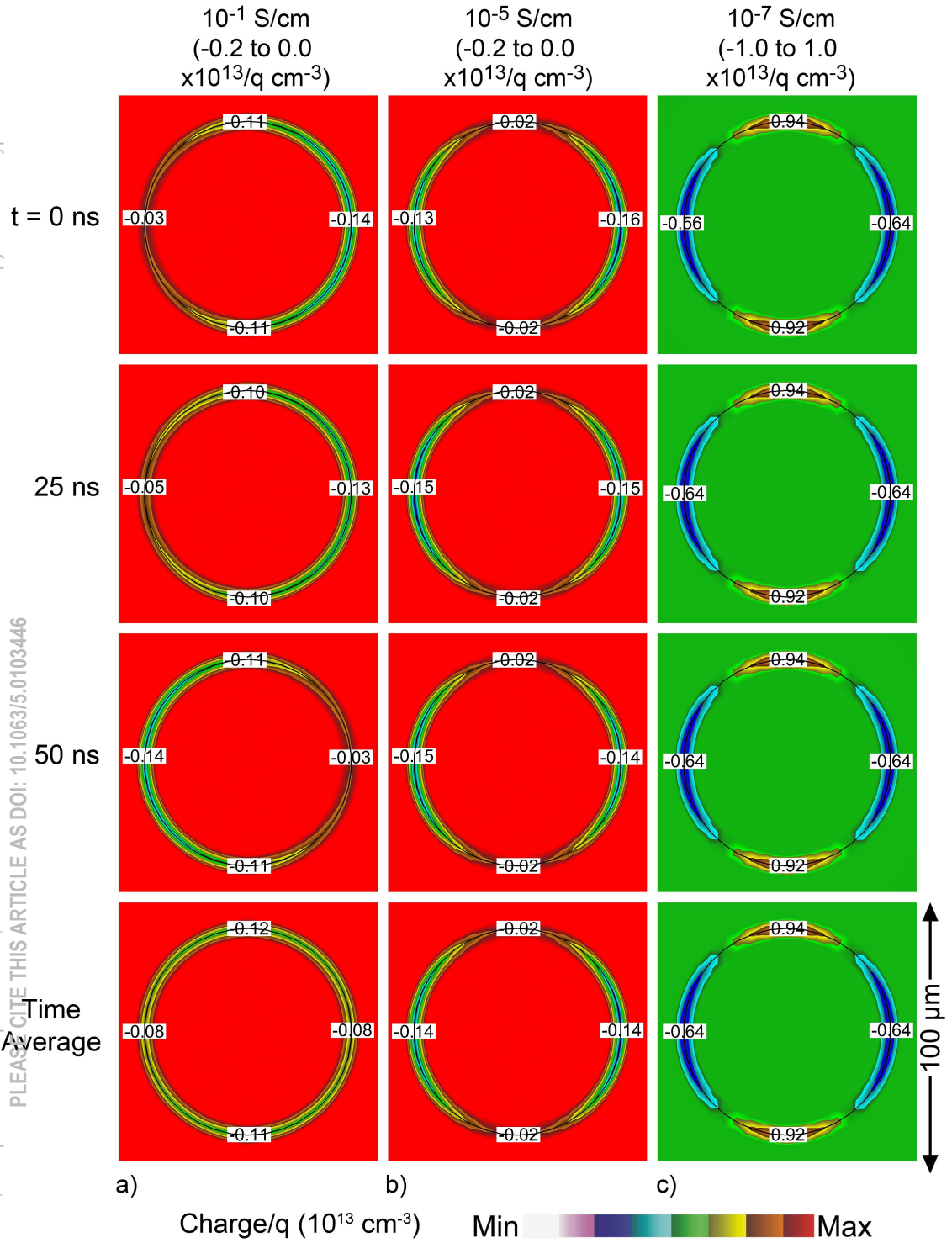

AIP Publishing

Journal of Applied Physics

ACCEPTED MANUSCRIPT

PLEASE CITE THIS ARTICLE AS DOI: 10.1063/5.0103446

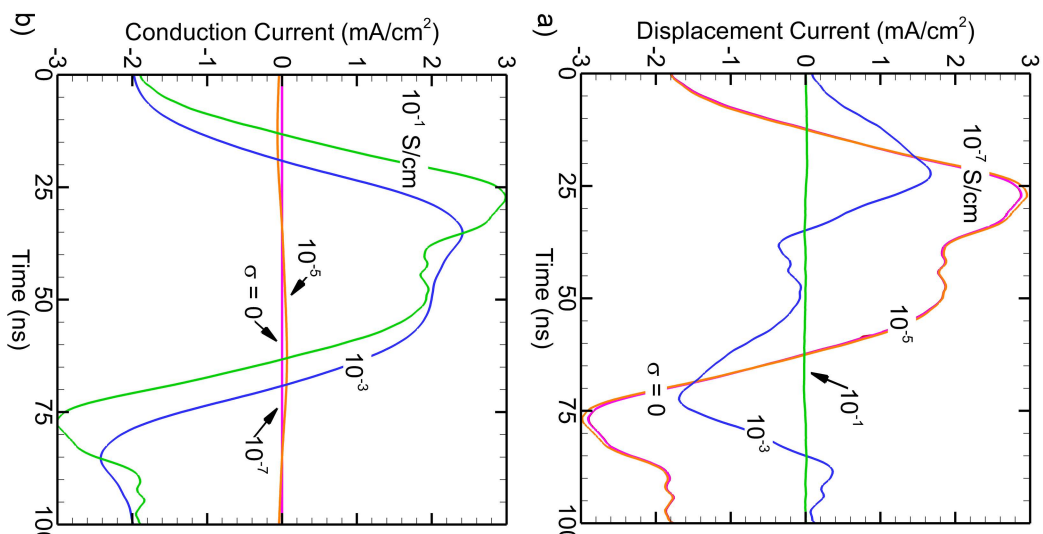

AIP Publishing

Journal of Applied Physics

ACCEPTED MANUSCRIPT

This is the author's peer reviewed, accepted manuscript. However, the online version of record will be different from this version once it has been copyedited and typeset.
PLEASE CITE THIS ARTICLE AS DOI: 10.1063/5.0103446

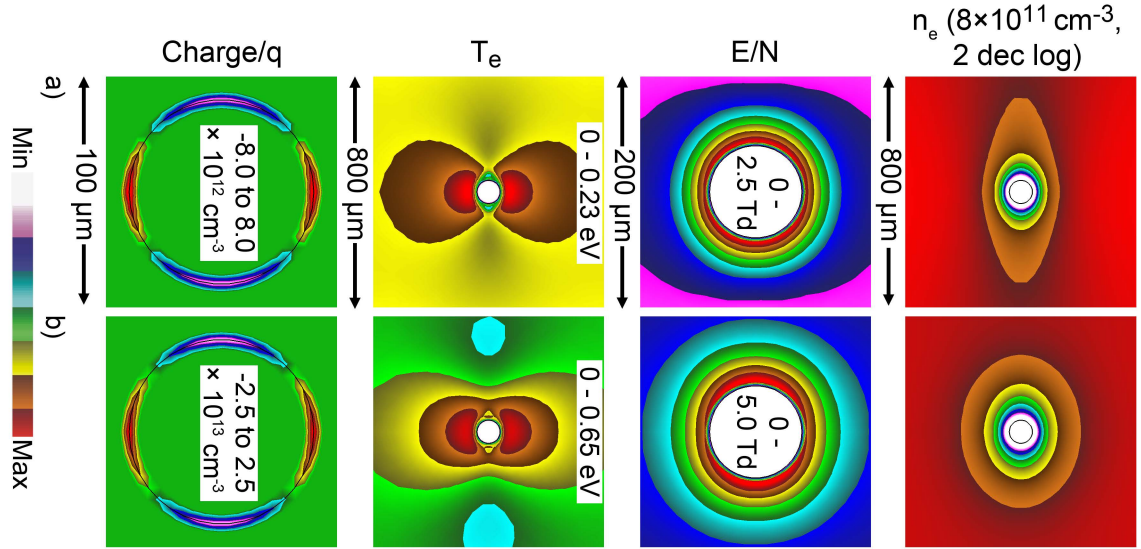

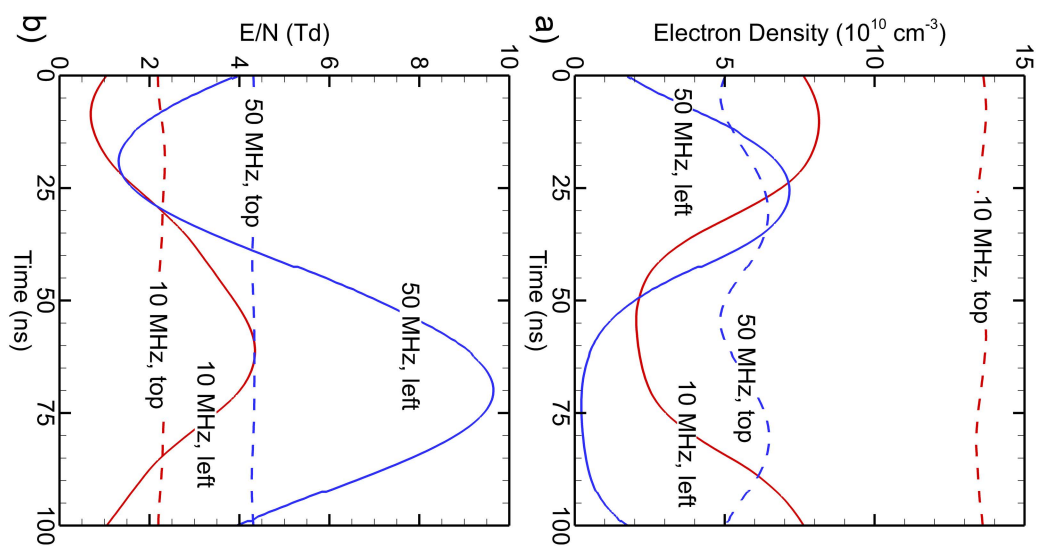

Journal of Applied Physics

PLEASE CITE THIS ARTICLE AS DOI: 10.1063/5.0103446

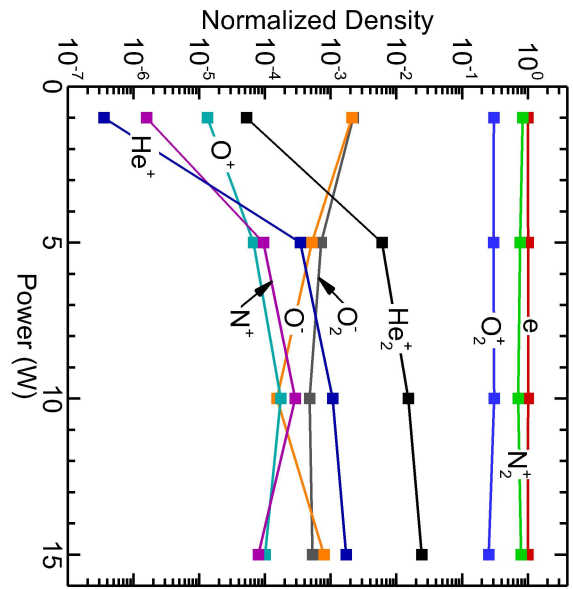

Journal of Applied Physics